



Effect of non-Heisenberg magnetic interactions on defects in ferromagnetic ironJacob B. J. Chapman ,* Pui-Wai Ma , and Sergei L. Dudarev*UK Atomic Energy Authority, Culham Science Centre, Oxfordshire OX14 3DB, United Kingdom* (Received 3 April 2020; revised 27 August 2020; accepted 3 November 2020; published 21 December 2020)

Fundamental flaws in the Heisenberg Hamiltonian are highlighted in the context of its application to bcc Fe, including the particular issues arising when modeling lattice defects using spin dynamics. Exchange integrals are evaluated using the magnetic force theorem. The bilinear exchange coupling constants are calculated for all the interacting pairs of atomic magnetic moments in large simulation cells containing defects, enabling a direct mapping of the magnetic energy onto the Heisenberg Hamiltonian and revealing its limitations. We provide a simple procedure for extracting the Landau parameters from density-functional theory calculations to construct a Heisenberg-Landau Hamiltonian. We quantitatively show how the Landau terms correct the exchange-energy hypersurface, which is essential for the accurate evaluation of energies and migration barriers of defects.

DOI: [10.1103/PhysRevB.102.224106](https://doi.org/10.1103/PhysRevB.102.224106)**I. INTRODUCTION**

Magnetism is a quantum mechanical phenomenon that arises from a combination of the Coulomb interaction between electrons and the Pauli exclusion principle. The spin state of the electrons affects the total energy through what is known as exchange interaction. In transition, rare earth, and actinide metals [1], electrides [2] and organic polyradicals [3], which all have partially filled *d* or *f* orbitals, magnetic moments are formed due to the exchange interaction between intra-atomic *d* or *f* electrons. Magnetism has been highly influential on modern technologies such as magnetic storage [4] and spintronic devices [5]. Exotic noncollinear spin textures such as skyrmions promise to revolutionize processor and data storage technologies further [6].

Iron-based alloys are particularly important industrial materials. They attain a myriad of complex magnetic states, such as ferro- and antiferromagnetic [7], incommensurate spin density waves [8–10] and spin-glasses [11,12]. Their mechanical properties are partially governed by the population of magnetic states [13,14]. For example, in pure iron, the softening of the tetragonal shear modulus *C'* near the Curie temperature *T_C* is driven by magnetism [15–17].

Body-centered cubic (bcc) crystal structure of iron owes its stability to the free energy contributions from both lattice and magnetic excitations [18–23]. Magnetism also makes the $\langle 110 \rangle$ dumbbell the most stable configuration of a self-interstitial atoms (SIA) in iron. This is in contrast to other nonmagnetic bcc transition and simple metals where a single SIA defect adopts a $\langle 111 \rangle$ or $\langle 11\chi \rangle$ configuration [24–26].

The Heisenberg Hamiltonian [27] is a well known model describing interaction between magnetic moments. It assumes that electrons are reasonably well localized, which is indeed the case in metals with *d* or *f* electrons. The Heisenberg

Hamiltonian can be written as

$$\hat{\mathcal{H}} = -\frac{1}{2} \sum_{ij} J_{ij}^{\text{eff}} \hat{\mathbf{s}}_i \cdot \hat{\mathbf{s}}_j, \quad (1)$$

where $\hat{\mathbf{s}}_i$ is a unit vector in the direction of an atomic spin $\mathbf{S}_i = S_i \hat{\mathbf{s}}_i$ at site *i*. J_{ij}^{eff} is an effective isotropic pairwise exchange coupling parameter describing interaction between spins at sites *i* and *j*. The local atomic magnetic moment and spin at site *i* are related simply by $\mathbf{M}_i = -g\mu_B \mathbf{S}_i$, where $g = 2.0023$ is the electron *g* factor and μ_B is the Bohr magneton.

In the Heisenberg approximation, parameters J_{ij}^{eff} govern the magnetic order, transition temperature, and magnon dispersion of the material [28–34]. The value of J_{ij}^{eff} can be estimated from experimental observations by fitting the temperature-dependent magnetic susceptibility curve [35,36]. On the other hand, J_{ij}^{eff} can be determined from density-functional theory (DFT) calculations [28,37,38].

There are two commonly used approaches to derive J_{ij}^{eff} from DFT calculations. The first is the real-space total energy method [39]. The total energy is evaluated for various metastable collinear magnetic configurations. The exchange coupling parameter is then estimated from the energy differences between various magnetic states.

This approach has several limitations. The necessity to perform total energy calculations for multiple configurations can be expensive in the limit of a large system size. This size problem cannot be circumvented for classes of materials such as organics or electrides [2]. In addition, the assumption that J_{ij}^{eff} is a simple scalar does not help deliver information about the contributing orbitals or the dominant mechanism of exchange interaction.

The second approach is known as the magnetic force theorem (MFT) [28–34,40–47]. It was first derived within the coherent-potential approximation (CPA) to analyze the high-temperature properties of itinerant magnetic systems [40–42]. Later, it was re-derived using multiple scattering theory to investigate the Ruderman-Kittel-Kasuya-Yoshida (RKKY)

*Corresponding author: jacob.chapman@ukaea.uk

interactions between impurities in metals [43]. The resultant expression for the exchange integrals is commonly referred to as the Lichtenstein-Katsnelson-Antropov-Gubanov (LKAG) equation [28]. This Green's function based approach provides an analytical expression for parameter J_{ij}^{eff} in the form of a response to the changes in the total energy resulting from small spin rotations in a particular magnetic state. Other complementary approaches to extract the magnetic exchange are also available, including the use of momentum-dependent irreducible susceptibilities within the framework of DFT+Dynamical Mean-Field Theory (DMFT). This is particularly applicable within and in the vicinity of the paramagnetic state of α -Fe [48,49].

The principal advantage of the MFT approach is that all the pairwise parameters J_{ij}^{eff} can be determined for a single magnetic configuration. The configuration does not need to be the true magnetic ground state, which may not be known. In addition, J_{ij}^{eff} may be decomposed into contributions from different orbitals [33,34,46].

Early developments of MFT were implemented using the localized orbital methods such as the linear muffin-tin orbital (LMTO) approach [38,50] and for the linear combinations of pseudoatomic orbitals (LCPAO) [46,47]. Recent extensions to plane-wave DFT codes have taken advantage of maximally localized Wannier functions [33].

Calculations of J_{ij}^{eff} are often motivated by the need to parametrize multiscale methods as the Heisenberg model approach can then be used to predict finite temperature properties of magnetic systems [20,23,23,51–54]. The studies performed using the MFT primarily concerned bulk materials or molecular magnets [28,29,55,56]. Defects [57,58] as well as nanostructures on substrates [59] have also been considered. Nonetheless, even for perfect crystalline configurations it has been observed that the adiabatic magnetic exchange-energy hypersurface parametrized by the bilinear Heisenberg Hamiltonian is incomplete [60–63]. An accurate representation necessitates longitudinal fluctuations to be considered [62,64,65].

Despite the known shortcomings of the Heisenberg Hamiltonian, it remains a popular choice for multiscale modeling. In this paper we address the consequences of the Heisenberg functional form of a magnetic Hamiltonian and show that applications of this Hamiltonian to distorted lattice configurations require extending it to the Heisenberg-Landau form [20,21,66,67]. We begin by benchmarking our density functional theory (DFT) calculations, performed using the OPENMX code [68], against the known literature and our in-house exchange coupling codes in Sec. III A. We then quantify the error of an idealized mapping of the DFT magnetic energy for pristine and defected configurations of body-centred cubic α -Fe in Sec. III B.

Our analysis in Sec. III C reveals that the magnetic hypersurface of point defects can be represented qualitatively, but the Heisenberg approximation fails to capture the relative stability of the $\langle 111 \rangle$ crowdion due to the mixed e_g - t_{2g} characteristic of the bands at the Fermi energy. We assert that even a perfectly mapped Heisenberg Hamiltonian is unable to predict point defect behavior in iron with reasonable quantitative reliability. In Sec. III D we demonstrate that a very accurate representation can be created by incorporat-

ing in the Hamiltonian the second- and fourth-order Landau coefficients. We provide a simple procedure showing how to extract atom-resolved Landau parameters from DFT calculations. This enables the itinerant behavior of d electrons to be incorporated into the magnetic model. Finally, in Sec. III E we explore the effect of magnetic interactions on the migration of a $\langle 110 \rangle$ self-interstitial atom defect.

II. METHODOLOGY

A. Simulation setup

We performed DFT calculations using the OPENMX package [68], which implements pseudopotentials and pseudoatomic orbitals. The bulk (pristine) simulation cell of Fe is constructed using $4 \times 4 \times 4$ unit cells containing 128 atoms. We use the Perdew-Burke-Ernzerhof (PBE) generalized gradient approximation exchange correlation functional [69,70], which together with the difference Hartree potential [71] are evaluated on a real space grid. Numerical integration of these nonlocal terms are performed upon the discrete real-space grid partitioned by a cutoff energy of 600 Ry.

The basis set is created via a linear combination of optimized pseudoatomic orbitals (LCPAO) [71–73], employing three s , three p , and three d orbitals centered on each atomic site, which all share a cutoff radius of 6 Bohr radii. Two-center integrals in the Kohn-Sham Hamiltonian evaluated in momentum space use $3 \times 3 \times 3$ k points constructed by the Monkhorst-Pack (MP) method [74]. We use the Fe pseudopotential of the form of Morrison, Bylander and Kleinman (MBK) [75,76] available within the OPENMX library, which include a nonlinear partial core correction. The separable form of the MBK pseudopotential is particularly suited for efficient LCPAO calculations. Ionic positions are relaxed until the maximum ionic force is smaller than 2×10^{-4} Ry/Bohr radius.

We performed benchmark tests against literature data. We calculated the lattice constants, elastic constants, and point defects formation energy and compared with data calculated by VASP [77–80] using the projector augmented wave (PAW) potential [26] and the ultrasoft pseudopotential (USPP) potential [81]. We checked the convergence of our data against the k -points density, electronic temperature, and real-space cutoff energy. Bulk properties of bcc and fcc phases are presented in Sec. III A. Defect formation energies are presented in Sec. III B. They all show good compatibility and confirm the validity of our results.

B. Exchange coupling parameter

The MFT [28] enables one to directly extract the scalar bilinear Heisenberg exchange integral J_{ij}^{eff} from electronic structure calculations. Here we address the Green's function formalism of the MFT [82,83]. The effective exchange integral can be written as

$$J_{ij}^{\text{eff}}(\mathbf{k}) = \frac{1}{\pi} \text{Im} \int_{-\infty}^{\epsilon_F} \text{Tr}(G_{\mathbf{k},ij}^{\uparrow\uparrow} \hat{V}_{\mathbf{k},i}^{\uparrow\uparrow} G_{\mathbf{k},ji}^{\downarrow\downarrow} \hat{V}_{\mathbf{k},j}^{\downarrow\downarrow}) d\epsilon. \quad (2)$$

The single-particle Greens function at a given energy ϵ is defined by the resolvent of the Kohn-Sham orbitals $|\phi_{\mathbf{k},i}^{\sigma}\rangle$ in

momentum space \mathbf{k} over the filled states:

$$G_{\mathbf{k},ij}^{\sigma\sigma}(\epsilon) = \sum_n \frac{|\phi_{\mathbf{k},i}^\sigma \langle \phi_{\mathbf{k},j}^\sigma |}{\epsilon - \epsilon_{\mathbf{k},n}^\sigma + i\eta}, \quad (3)$$

where the spin index σ for our collinear calculations refers to the majority \uparrow and minority \downarrow spins, $\epsilon_{\mathbf{k},n}^\sigma$ is the n th eigenenergy, and η is a positive infinitesimal smearing factor, implying the limit $\eta \rightarrow 0$.

The philosophy leading to the derivation of the MFT presents that a good and convenient way to determine the electronic structure of a system is to work within the grand canonical potential (GCP). One is then able to relate variations in the GCP to changes in the integrated density of states. In turn, using Lloyd's formula [84], the integrated density of states may be expressed by a transition matrix which relates states of the perturbed system to the states of the unperturbed Hamiltonian. This may be represented as an open Born series constructed from successive expansions of retarded Green's functions of the unperturbed states [Eq. (3)] and an on-site scattering potential $[\hat{V}_i^{\uparrow\downarrow}]$, Eq. (4). As a result, changes in the GCP owing to a small spin rotation can ultimately be determined by knowing the relevant on-site potential. This is taken to be the potential difference induced by the rotation of the magnetic moment.

For collinear spins, the off-diagonal components of a local Hamiltonian $H_i^{\uparrow\downarrow}$ and $H_i^{\downarrow\uparrow}$ representing a given atomic site i are zero. The on-site exchange splitting potential $\hat{V}_{\mathbf{k},i}^{\uparrow\downarrow}$ at atomic site i due to an infinitesimal spin rotation can then be approximated using the difference in the local Hamiltonian between the up and down spin channels [47,82]:

$$\hat{V}_{\mathbf{k},i}^{\uparrow\downarrow} = \frac{1}{2} \left(\hat{H}_{\mathbf{k},i}^{\uparrow\uparrow} - \hat{H}_{\mathbf{k},i}^{\downarrow\downarrow} \right). \quad (4)$$

The local Hamiltonian is the partial matrix of the full Kohn-Sham Hamiltonian representing site i . Since our LCPAO calculations are using three s , three p , and three d orbitals per Fe atom, the local Hamiltonian matrices have 27×27 matrix elements per spin state accessed via orbital indices.

Finally, within the LKAG formulation one can relate the changes to the GCP to the bilinear exchange parameters by means of Eq. (2). Detailed derivations can be found in Refs. [28,45]. We present now the practical implementation of the MFT as used in the current work.

For nonorthogonal LCPAO basis used in OPENMX, the MFT within the rigid spin approximation with noncollinear magnetic perturbations can be reexpressed in a practical manner as shown in Ref. [47] by Han *et al.* More recently, the same expression has been rederived using local projection operators [29]. In the orbital representation,

$$J_{ij}^{\text{eff}}(r_{ij}) = \frac{1}{4} \int d\mathbf{k} \sum_{\alpha,\beta} \left(\frac{f_\alpha^\uparrow - f_\beta^\downarrow}{\epsilon_\beta^\downarrow - \epsilon_\alpha^\uparrow + i\eta} \right) \times \sum_{a,b}^{N_i} C_{\mathbf{k},\alpha a}^\uparrow \hat{V}_{ab}^{\uparrow\downarrow} C_{\mathbf{k},\beta b}^\downarrow \sum_{a',b'}^{N_j} C_{\mathbf{k},\alpha a'}^\uparrow \hat{V}_{a'b'}^{\uparrow\downarrow} C_{\mathbf{k},\beta b'}^\downarrow, \quad (5)$$

where the indices a and b run over the pseudoatomic orbitals centered on site i , and a', b' span over site j . α, β are indices spanning all the orbitals in the system. f_α^\uparrow and f_β^\downarrow are the Fermi distributions:

$$f_\alpha^\sigma = \frac{1}{1 + \exp[(\epsilon_\alpha^\sigma - \mu)/k_B T]}, \quad (6)$$

with electron smearing temperature T and chemical potential μ . $\hat{V}_{ab}^{\sigma\sigma'}$ is the matrix element for the on-site potential at site i between the orbitals centered at that site indexed a and b . $C_{\alpha a}^\sigma$ are the molecular orbital coefficients of the self-consistently solved generalized Kohn-Sham equations:

$$\mathbf{H}\mathbf{C}_\alpha = \epsilon_\alpha \mathbf{S}\mathbf{C}_\alpha, \quad (7)$$

where $\mathbf{C}_\alpha = (C_{\alpha 1}, C_{\alpha 2}, \dots, C_{\alpha N_i})^T$. This vector is constructed using a Löwdin transformation with the unitary vectors \mathbf{U} that diagonalize the overlap of the Kohn-Sham orbitals \mathbf{S} . The corresponding eigenvalues \mathbf{e} are necessarily positive definite. The transformation is then expressed as

$$\mathbf{C}_\alpha = \frac{1}{\sqrt{e_\alpha}} \mathbf{U}_\alpha^\dagger \mathbf{H}\mathbf{U}_\alpha \frac{1}{\sqrt{e_\alpha}}. \quad (8)$$

Since Eq. (8) is a matrix equation, the identical positive definite terms involving the inverse square root of the overlap eigenenergies are noncommutative.

The exchange coupling parameter J_{ij}^{eff} can then be calculated within the framework of DFT. OPENMX [68] provides a utility that calculates J_{ij}^{eff} . However, it was primarily developed for calculation of molecules. Instead of using it, we developed our own code that has been optimized for bulk materials. We note that recently a new release of OPENMX became available containing improvements to the exchange coupling code [85].

In order to treat the variable magnitude of atomic spin, which we discuss below, we define another Heisenberg Hamiltonian \mathcal{H} :

$$\mathcal{H} = -\frac{1}{2} \sum_{ij} J_{ij} \mathbf{S}_i \cdot \mathbf{S}_j, \quad (9)$$

where \mathbf{S}_i is the atomic spin vector at site i and J_{ij} is the exchange coupling parameter. In the Heisenberg Hamiltonian defined in Eq. (1), the magnitude of the atomic spins are subsumed into J_{ij}^{eff} . Comparing Eqs. (1) and (9), the two exchange parameters are related by

$$J_{ij} = \frac{g^2 \mu_B^2}{M_i M_j} J_{ij}^{\text{eff}}. \quad (10)$$

The magnetic moments \mathbf{M}_i can be determined by a Mulliken population analysis of the electronic density and overlap matrices:

$$M_{\sigma,i\alpha} = \sum_n \sum_{j\beta} \rho_{\sigma,i\alpha j\beta}^{(\mathbf{R}_n)} S_{i\alpha j\beta}^{(\mathbf{R}_n)}, \quad (11)$$

where $\rho_{\sigma,i\alpha j\beta}^{(\mathbf{R}_n)}$ is the density matrix pertaining to the periodic image of the simulation cell whose origin is positioned at \mathbf{R}_n . $S_{i\alpha j\beta}^{(\mathbf{R}_n)}$ is the overlap matrix. Indices i and j refer to the atomic sites, α and β are the orbital indices, σ denotes spin, and n spans the periodic images of the simulation cell within a given cutoff radius.

TABLE I. Ground-state properties of bcc Fe as calculated using the OPENMX [68], compared with plane-wave DFT calculations using VASP [26] and experiment.

Property	OPENMX (Present)	VASP [26]	Expt.
a_0 (Å)	2.842	2.831	2.87 [86]
$\langle M \rangle$ (μ_B)	2.25	2.21	2.22 [7]
Ω_0 (Å ³)	11.49	11.34	11.82 [86]
C_{11} (GPa)	242.12	289.34	243.1 [87]
C_{22} (GPa)	138.74	152.34	138.1 [87]
C_{44} (GPa)	87.72	107.43	121.9 [87]

III. RESULTS

A. Bulk iron

We compare our bulk Fe data with other DFT calculations. The data in Table I, produced using OPENMX calculations, show excellent agreement with other similar studies. The ground state of iron is, as expected, found to be the bcc ferromagnetic (α) phase with atomic magnetic moments of $2.22\mu_B$, in agreement with experiment [86].

The equilibrium lattice parameter $a_0^{\text{DFT}} = 2.842$ Å is slightly underestimated relative to the experimental value $a_0^{\text{exp}} = 2.8665$ Å. This is not unexpected as overbinding effects are relatively common in the context of DFT calculations.

The lowest energy magnetic configuration in the fcc phase is double-layer antiferromagnetic (AF2), which is 0.1 eV higher in energy than the FM bcc α phase. They are consistent with Ref. [23]. We notice a small discrepancy in the stability of the fcc magnetically ordered phases (Table II). Our calculations find the next stable configurations to be the high-spin ferromagnetic (HS) and single-layer antiferromagnetic (AF1), which are nearly degenerate at 0.12 and 0.13 eV, respectively. This differs from Ref. [23] where the stability was explored using the PAW method. The AF1 phase was found to be the next stable phase, with the HS and ferromagnetic low spin (LS) configurations being of comparable stability. This difference likely arises from differences between the pseudopotentials used in the two approaches.

In Fig. 1 we plot the magnitude of the magnetic moments as a function of volume for different magnetically ordered phases. We find quantitative agreement with previous

TABLE II. Comparison of the ground state fcc Fe magnetic structures calculated with OPENMX with reference data. Reference DFT data were collected from Ref. [89] unless stated otherwise. Atomic volumes Ω_0 are given in Å³. Values in the last column represent the difference between the energy per atom computed for a given structure and the energy per atom in the ferromagnetic bcc phase. Values as functions of volume are plotted in Fig. 1.

Configuration	Ω_0 (Å ³) (Present)	Ω_0 (Å ³) (Ref.)	$\langle M \rangle$ (μ_B) (Present)	$\langle M \rangle$ (μ_B) (Ref.)	Energy diff. (eV) (Present)
AF1	11.05	10.76, 11.37 [90]	2.00	1.574	0.13
AF2	11.50	11.20	2.376	2.062	0.096
FM-HS	12.14	11.97, 12.12 [90]	2.631	2.572	0.12
FM-LS	10.84	10.52	1.324	1.033	0.21
NM	10.38	10.22	0.000	0.000	0.25

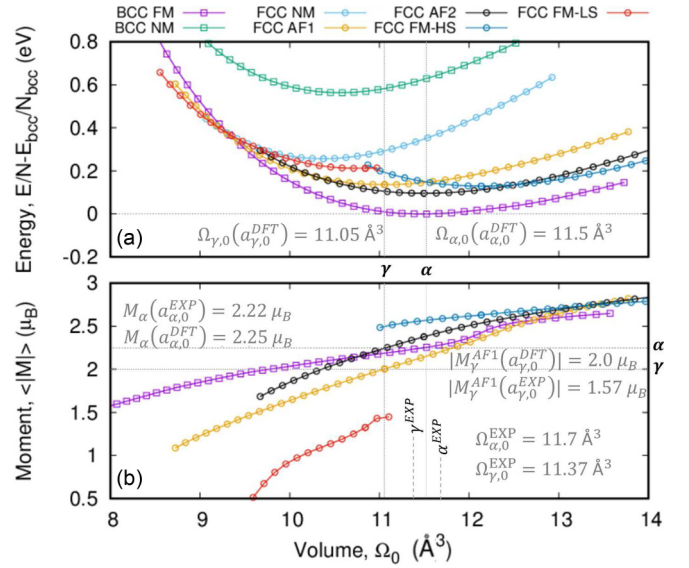


FIG. 1. (a) Energy and (b) magnitude of magnetic moment of different magnetic configurations of bcc and fcc Fe calculated using OPENMX. Energies are normalized per atom and are shown relative to the global 0 K ground state (bcc FM). Atomic volume Ω_0 is computed as the total volume of the simulation cell divided by the number of atoms in it, $|\langle \vec{L}_x \times \vec{L}_y \rangle \cdot \vec{L}_z|/N$. The following magnetic configurations are shown for α -Fe and γ -Fe: bcc ferromagnetic (FM), bcc nonmagnetic (NM), fcc nonmagnetic (NM), fcc high-spin (HS), fcc low-spin (LS), fcc antiferromagnetic (AF1), and fcc double-layer antiferromagnetic (AF2). Further properties for the relaxed structure of each magnetic configuration are provided in Tables I and II for α -Fe and γ -Fe, respectively.

calculations showing that the magnitude of the moments decreases under compression due to the increasing exchange energy to satisfy the Pauli exclusion principle. We also observe an inflection point in the α phase when, under tension, the lattice parameter of $1.014a/a_0^{\text{DFT}}$ (where $\Omega_0 \approx 12$ Å³ in Fig. 1) is reached. This kinking is known to occur due to large changes in the t_{2g} density of states at the Fermi level ϵ_F relative to smaller changes in the density of states associated with the e_g orbitals [88].

Values of the exchange coupling parameter J_{ij}^{eff} of bcc ferromagnetic Fe calculated using the MFT [28] [Eq. (5)] are given in Table III. The values were computed assuming the experimentally observed lattice parameter, or the lattice param-

TABLE III. Values of effective exchange coupling parameters J_{ij}^{eff} evaluated using the magnetic force theorem. Values of J_{ij}^{eff} were computed assuming the experimental lattice parameter $a_0^{\text{exp}} = 2.8665 \text{ \AA}$ or the DFT equilibrium lattice parameter $a_0^{\text{DFT}} = 2.842 \text{ \AA}$ (in parentheses). The Curie temperature T_C can be estimated in the mean field approximation using Eq. (12). We included contributions from the four nearest neighbor shells, where in the bcc case $T_C \approx 2(8J^{(1)} + 6J^{(2)} + 12J^{(3)} + 24J^{(4)})/3k_B$.

J_{ij}^{eff} (mRy)	LCPAO (GGA) (Present)	LMTO (GGA) [88]	LMTO (LSDA) [91]	LMTO (LSDA) [50]
$J^{(1)}$	1.204 (1.14)	1.218	1.24	1.212
$J^{(2)}$	0.953 (0.72)	1.08	0.646	0.593
$J^{(3)}$	-0.035 (-0.004)	-0.042	0.007	0.018
$J^{(4)}$	-0.085 (-0.087)	-0.185	-0.108	-0.07
J_0^{eff}	12.89 (11.30)	11.28	11.03	11.79
T_C (K)	1362 (1193)	1186	1170	1240

eter corresponding to the DFT energy minimum (values given in parentheses). The table gives the values of exchange parameters computed for the first four nearest neighbor shells; the corresponding values are denoted as $J^{(1)}$, $J^{(2)}$, $J^{(3)}$, and $J^{(4)}$.

Two recent studies performed using the LMTO [33] and LCPAO [46] tested the dependence of the computed values of exchange parameters on the choice of the basis set. Depending on the choice of basis functions, the calculated values of exchange parameters J_{ij}^{eff} can vary by 3 meV (0.2 mRy). It has also been noted that DMFT corrections affect the magnitude of orbitally resolved $J_{ij}^{\text{eff}}(r_{ij})$, but the sign and relative strength remain unaltered [30]. It suggests that, while we could opt for a more sophisticated method, our results summarized in Table III are informative and show good compatibility with published data [50,88,91].

We explored the variation of the effective exchange coupling parameter $J_{ij}^{\text{eff}}(r_{ij})$ treated as a function of interatomic distance r_{ij} by varying the volume of the simulation cell. The linear dimension of the cell varied in the range of $\pm 3\%$. Figure 2 shows the calculated exchange coupling parameter J_{ij} defined according to Eq. (10). Again, the data agree with the results from Ref. [23], where the calculations were performed using the LMTO Green's function technique, developed and implemented by van Schilfgaarde *et al.* [28,38].

Using the values J_{ij}^{eff} computed for several coordination shells, the T_C can be estimated in the mean field approximation [28] as

$$k_B T_C \approx \frac{2}{3} J_0^{\text{eff}}, \quad (12)$$

where $J_0^{\text{eff}} = \sum_{j \neq 0} J_{0j}^{\text{eff}}$. The data given in Fig. 2 show that $J^{(1)}$ and $J^{(2)}$ give the dominant contribution to J_0^{eff} . Still, we evaluate J_0^{eff} using the effective exchange parameters for the coordination shells extending to the fourth nearest neighbor. The estimated values of T_C are given in Table III together with other values, taken from literature and also calculated in the mean field approximation.

Mean field Curie temperatures are known to overestimate the experimentally measured values by 15–30%. This is due to the MFA's inaccurate treatment of the correlation between spins. For the DFT equilibrium lattice parameter a_0^{DFT} the T_C in the MFA is calculated as 1362 K, which is consistent

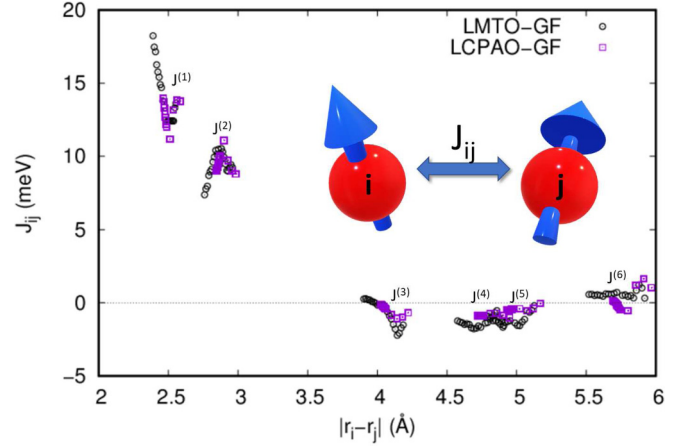


FIG. 2. The exchange coupling parameter J_{ij} as a function of interatomic distance. Black circles are data from Ref. [23], calculated using the LMTO-GF method [28,38]. Purple squares are the current results calculated using LCPAO and the MFT [28] [Eq. (5)], where the volume of a simulation box containing 128 atoms varies such that the linear dimension change is in the range of $\pm 3\%$.

with other LCPAO and KKR calculations [85]. Factoring the known overestimation of MFA, it is in reasonable agreement with the experimental $T_C = 1043 \text{ K}$. When the magnetic exchanges are recalculated at the experimental lattice parameter as provided in parenthesis in Table III, the T_C in the MFA becomes consistent with experiment. However, due to overbinding within the DFT calculations, recalculation at the experimental lattice parameter (2.8665 \AA) reduces the overlap of the d -band electrons which in turn reduces the exchange contribution due to Eq. (8). The noted lowering of the calculated T_C is therefore a consequence of an underestimation of the exchange integral.

B. Point defects in iron

We now investigate magnetic interactions in iron containing point defects, and compare the results to the bulk case. First, we benchmark the calculated formation energy of a self-interstitial atom (SIA) defect and a vacancy against literature data [81,92–94]. Then, we study how the exchange coupling parameters vary in the vicinity of a defect, especially near the core of a defect configuration.

The formation energy E_{def}^F of a defect formed in a given structural and magnetic phase can be written as

$$E_{\text{def}}^F = E_{\text{def}}(N_{\text{def}}) - \frac{N_{\text{def}}}{N_{\text{bulk}}} E_{\text{bulk}}(N_{\text{bulk}}), \quad (13)$$

where $E_{\text{def}}(N_{\text{def}})$ is the energy of a system including the defect and $E_{\text{bulk}}(N_{\text{bulk}})$ is the energy of the reference perfect system. The number of atoms in each system is N_{def} and N_{bulk} , respectively. For the cell size and defect structures considered here we ignore the elastic correction to the formation energy of the defect [26], as the magnitude of the elastic correction varies between 0.2 and 0.3 eV whereas the variation of DFT parameters leads to an absolute error in the formation energy of the order of 0.05–0.1 eV per SIA [95], which is a quantity of similar magnitude.

The simulation cell for a defect calculation is chosen to be of the same shape and volume as in the perfect lattice

TABLE IV. Calculated defect formation energies E_{def}^f . Calculations were performed using a LCPAO basis set. Our results are compared with Refs. [26,81,92,93] where calculations were performed using LCPAO, plane wave with PAW, or plane wave with USPP. Values in parentheses show the energy difference of an SIA configuration with respect to the formation energy of a $\langle 110 \rangle$ dumbbell. Due to the short range of the LCPAO, we present the calculated formation energy of a vacancy with (dagger) and without the additional basis functions added to the vacancy site. All the calculations were performed using 128 ± 1 atom cells. Units are in eV.

Defect	PAO (Present)	PAW [81]	PAO [93]	USPP [81]	PAW [26]
$\langle 110 \rangle_D$	4.49	4.02	3.64	3.94	4.42
Tetrahedral	4.98 (0.49)	4.44 (0.42)	4.26 (0.62)	4.46 (0.52)	4.88 (0.46)
$\langle 111 \rangle_D$	5.25 (0.81)		4.34 (0.70)	4.66 (0.72)	5.21 (0.79)
$\langle 111 \rangle_C$	5.27 (0.79)	4.72 (0.70)			5.21 (0.79)
$\langle 100 \rangle_D$	5.58 (1.10)	5.13 (1.11)	4.64 (1.00)	5.04 (1.10)	5.59 (1.17)
Octahedral	5.74 (1.25)	5.29 (1.27)	4.94 (1.30)	5.25 (1.31)	5.68 (1.26)
Vacancy	2.26 / 2.18 [†]	2.15	2.07	2.02	2.19

case. SIA configurations are created by inserting additional Fe atoms at different positions in the lattice, and all the ionic positions are then relaxed until all the forces acting on ions are lower than 2×10^{-4} Ry/Bohr radius. We considered the self-interstitial atom (SIA) configurations including $\langle 100 \rangle$, $\langle 110 \rangle$ and $\langle 111 \rangle$ dumbbell, $\langle 111 \rangle$ crowdion, tetrahedral site interstitial, and octahedral site interstitial. A vacancy configuration is created by removing an atom, followed by relaxation of ionic positions.

The formation energies of point defects in bcc Fe are summarized in Table IV, and compared with results given in Refs. [26,81,93]. The most stable SIA configuration is the $\langle 110 \rangle$ dumbbell, which agrees with earlier results [24,25,92,93]. The relative stability also follows the same order, such that the formation energies are ordered as $\langle 110 \rangle_D <$ tetrahedral $<$ $\langle 111 \rangle_C <$ $\langle 111 \rangle_D <$ $\langle 100 \rangle_D <$ octahedral, where the corresponding configurations are 0.49, 0.79, 0.81, 1.10, and 1.25 eV higher in energy than the $\langle 110 \rangle$ dumbbell, respectively. Subscripts D and C denote dumbbell and crowdion configurations. Our results agree well with the literature data derived using different basis sets and pseudopotentials.

The magnetic moments of SIA configurations are also consistent with those reported in literature [81,92]. In general, the magnetic moments in the core of an SIA configuration are significantly suppressed. Moments at the tensile first nearest neighbor (n.n.) sites are enhanced while those at sites characterized by a compressive strain are slightly decreased relative to the bulk value. A more complex relation between the local structure and local magnetic moment was found in $C15$ defect clusters [96].

In the case of a $\langle 110 \rangle_D$, the magnetic moments of the two Fe atoms at the core of the defect are antiparallel with respect to the surrounding atoms, and the magnitude of both magnetic moments is $-0.30\mu_B$. This is slightly larger than what is found in calculations performed using the PAW method, which predicts the value of $-0.1\mu_B$ [26], and using USPP, which gives $-0.2\mu_B$ [81].

In the case of a $\langle 111 \rangle_D$, the two core atoms are in the ferromagnetic state having moments of $+0.19\mu_B$. In Ref. [81], the two core atoms can be ferromagnetic ($0.3\mu_B$) or anti-ferromagnetic ($-0.5\mu_B$), if the USPP or PAW method is used, respectively. These results are in good agreement with

literature data. We now move on to the calculations of the exchange coupling parameters.

In Fig. 3, we present both the effective exchange coupling parameter J_{ij}^{eff} (Eq. 5) and the exchange coupling parameter J_{ij} (Eq. 10) computed for various SIA and vacancy configurations. J_{ij}^{eff} at around the perfect lattice first n.n. distance has magnitude in the range of 15–25 meV, whereas its value in a perfect lattice is 19 meV. Both J_{ij}^{eff} and J_{ij} tail off quickly

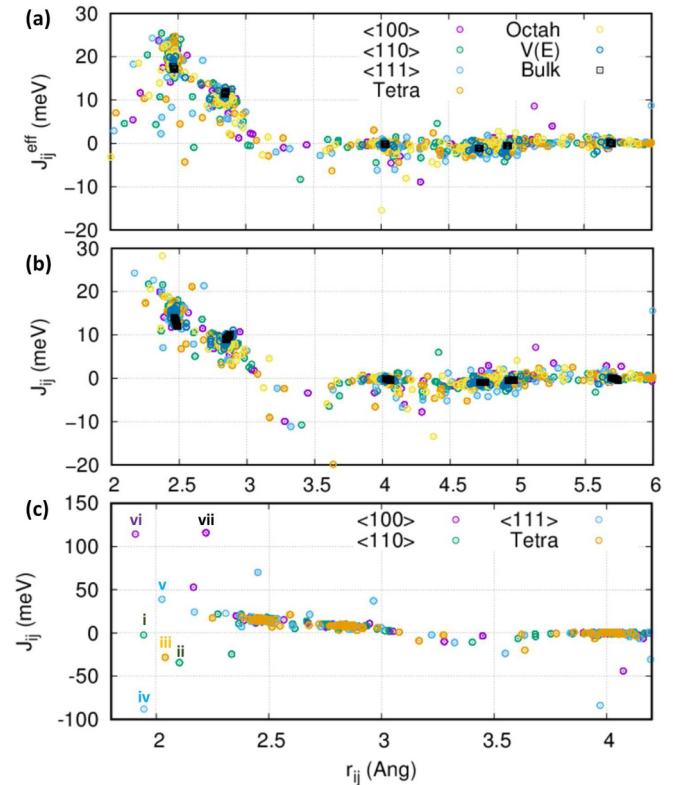


FIG. 3. (a) J_{ij}^{eff} [Eq. (5)] and (b) J_{ij} [Eq. (10)] as a function of interatomic distance $r_{ij} = |\mathbf{r}_i - \mathbf{r}_j|$ for SIA defects, including $\langle 100 \rangle$, $\langle 110 \rangle$, $\langle 111 \rangle$ dumbbells, a tetrahedral site interstitial, an octahedral site interstitial, and a vacancy configuration. Bulk values are also shown for comparison. (c) J_{ij} shown over a greater ordinate range to include the outliers.

TABLE V. Exchange coupling parameters between a core atom (α) and its first nearest neighbors (β). Multiplicity is defined per α atom. The key identifies specific data point plotted in Fig. 3(c). We indicate whether the exchange coupling parameter contributes to increase (\uparrow) or decrease (\downarrow) the energy of the system.

SIA	Key	Pair	M (μ_B)	Order	Multiplicity	J^{eff} (meV)	J (meV)
$\langle 110 \rangle_D$	i	$J_{\alpha\alpha}$	$M_\alpha = -0.304$	FM	1	-0.05	-2 (\uparrow)
	ii	$J_{\alpha\beta}$	$M_\beta = +1.75$	AFM	2	19.6	-35 (\downarrow)
Tetrahedral	iii	$J_{\alpha\beta}$	$M_\alpha = -0.87$ $M_\beta = +1.13$	AFM	4	6.8	-28(\downarrow)
	iv	$J_{\alpha\alpha}$	$M_\alpha = +0.198$	FM	1	-0.84	-88 (\uparrow)
$\langle 111 \rangle_D$	v	$J_{\alpha\beta}$	$M_\beta = +1.49$	FM	1	3.00	+38 (\downarrow)
	vi	$J_{\alpha\alpha}$	$M_\alpha = +0.188$	FM	1	1.0	+114 (\downarrow)
$\langle 100 \rangle_D$	vii	$J_{\alpha\beta}$	$M_\beta = +2.14$	FM	4	11.6	+116 (\downarrow)

by the third n.n., where $r_{ij} \approx 4 \text{ \AA}$. The exchange coupling parameter depends on the overlap between the localized basis functions, and so decays rapidly. Despite overlapping with orbitals of the core atoms, the values of J_{ij}^{eff} do not change much for bulk-like atoms surrounding the defect core. One can expect the bulk exchange coupling parameters to be a good approximation to them.

Here we introduce the notation α , β , and γ as dummy indices representing the index of the core atoms, and their first and second n.n., respectively. For the first and second n.n. of the core atoms, where there is a greater degree of orbital overlapping, J_{ij}^{eff} behaves as in a glassy material with scattered values $-0.5 < J_{\alpha\beta}^{eff} < 27$ meV. If we look at J_{ij} [Eq. (10)] instead, the magnitudes of $J_{\alpha\alpha}$ and $J_{\alpha\beta}$ are 2 to 5 times greater than for the bulk first n.n. interaction, as shown in Fig. 3(c).

In Table V, values of parameters $J_{\alpha\alpha}$ and $J_{\alpha\beta}$ are presented for the $\langle 100 \rangle_D$, $\langle 110 \rangle_D$, $\langle 111 \rangle_D$, and tetrahedral site interstitials. They are also shown in Fig. 3(c) via the key indexes. We can understand that the suppression of the magnetic moment of the core atoms is responsible for the large increase in J_{ij} between the core and proximate neighbors, which occurs due to the fact that $J_{ij} \propto 1/M_i M_j$.

Exchange interactions may increase or decrease the energy of a system. According to the definition of the Heisenberg Hamiltonian [Eq. (9)], aligned spins ($\mathbf{M}_i \cdot \mathbf{M}_j > 0$) with $J_{ij} > 0$ will lower the energy. On the other hand, if $J_{ij} < 0$, the antiparallel orientation of moments is favorable. In most cases, the magnetic energy of α - α and α - β exchange interactions acts to lower the energy. The $\langle 111 \rangle_D$ is an exception. The magnetic interaction between the two core atoms increases the energy by almost 0.9 eV for each core atom. When considering all interactions in the $\langle 111 \rangle_D$ system the exchange energy still acts to lower the total energy. However, due to these large positive contributions the total energy is reduced by less than the other defect configurations. This results in a change in the order of stability relative to *nonmagnetic* iron (see Table IV and Sec. III C). This observation agrees with previous studies [24,26] suggesting that magnetism is responsible for $\langle 110 \rangle_D$ being more stable than the $\langle 111 \rangle_D$ in contrast to other bcc metals.

C. Failure of the Heisenberg Hamiltonian

For a fixed atomic configuration $\mathcal{R} = \{\mathbf{r}_i\}$, we may calculate the energy change due to a specific spin ordering $\mathcal{S} =$

$\{\mathbf{S}_i\}$. We may define the magnetic contribution to energy as the difference between the magnetic and nonmagnetic states of configuration \mathcal{R} :

$$E_{MC}^{DFT}(\mathcal{R}, \mathcal{S}) = E_M^{DFT}(\mathcal{R}, \mathcal{S}) - E_{NM}^{DFT}(\mathcal{R}), \quad (14)$$

where E_M^{DFT} and E_{NM}^{DFT} are the cohesive energies calculated with and without spin polarization from DFT, respectively.

Using the MFT [28], we aim to map the DFT magnetic energy contribution onto the Heisenberg functional form. We note that the MFT is derived using relations from the second derivative of the energy with respect to the atomic spin:

$$\frac{\partial^2 E_{MC}^{DFT}}{\partial \mathbf{S}_i \partial \mathbf{S}_j} = \frac{\partial^2 E_M^{DFT}}{\partial \mathbf{S}_i \partial \mathbf{S}_j} \approx -J_{ij}. \quad (15)$$

If $E_{MC}^{DFT}(\mathcal{R}, \mathcal{S})$ varies approximately the same as the Heisenberg Hamiltonian E_{MC}^{HH} , the system can be said to be a good *Heisenberg magnet*.

In Table VI, we list the contributions of each term in Eq. (14). The nonmagnetic calculations were performed using the relaxed atomic configuration from the corresponding spin-polarized calculation. The use of non-spin-polarized calculation changes the order of stability of SIAs. It decreases the energy of the $\langle 111 \rangle_D$ relative to the tetrahedral site interstitial. This is consistent with the values of exchange coupling parameters between the core atoms and their neighbors of the $\langle 111 \rangle_D$, which increases the energy (Table V).

On the other hand, the energy of the $\langle 100 \rangle_D$ in the nonmagnetic calculations increases relative to the $\langle 110 \rangle_D$ by 0.3 eV. Despite the 0.1 eV magnetic contributions between each of the α and β ions, which lower the energy significantly, the $\langle 100 \rangle_D$ remains energetically unfavorable.

As a brief note, one may consider the relaxation of defect structures directly using non-spin-polarized DFT to determine the nonmagnetic order of stability. However, we find that these structures have negative tetragonal shear moduli and are therefore mechanically unstable.

Provided that $E_{MC}^{DFT} \approx E_{MC}^{HH}$, one may approximate the total magnetic energy using the Heisenberg Hamiltonian as

$$E_M^{DFT}(\mathcal{R}, \mathcal{S}) \approx E_{MC}^{HH}(\mathcal{R}, \mathcal{S}) + E_{NM}^{DFT}(\mathcal{R}), \quad (16)$$

as one may wish to achieve in a multiscale model.

From Table VI, we observe that E_{MC}^{HH} and E_{MC}^{DFT} differ by about 4 Ry. In terms of the relative energy difference with respect to the $\langle 110 \rangle_D$, the most deviated case is the $\langle 111 \rangle_D$.

TABLE VI. Calculated values of various energy terms computed for simulation cells containing relaxed SIA configurations (in Rydberg units). We record them as cohesive energies, shifted relative to the energy of the ground state bcc structure ($E = E^{\text{calc}} - N_{\text{atom}}E_{\text{ref}}^{\text{bcc}}$). Energy differences with the $\langle 110 \rangle_D$ configuration are given in parentheses in units of eV. Subscripts correspond to the following nomenclature: M = cohesive energy in a spin-polarized calculation, NM = cohesive energy in a non-spin-polarized calculation, MC = magnetic contribution, HH = Heisenberg Hamiltonian, and HL = Heisenberg-Landau Hamiltonian. Further, we may define the energy terms as $E_{\text{MC}}^{\text{DFT}} = E_{\text{M}}^{\text{DFT}} - E_{\text{NM}}^{\text{DFT}}$, $E_{\text{M}}^{\text{HH}} = E_{\text{NM}}^{\text{DFT}} + E_{\text{MC}}^{\text{HH}} = E_{\text{NM}}^{\text{DFT}} + \mathcal{H}$, $E_{\text{M}}^{\text{HL}} = E_{\text{NM}}^{\text{DFT}} + \mathcal{H}_L$.

	$\langle 110 \rangle_D$	Tetrahedral	$\langle 111 \rangle_D$	$\langle 100 \rangle_D$
$E_{\text{M}}^{\text{DFT}}$	0.3298	0.3657 ($\Delta_{110} = 0.49$ eV)	0.3879 ($\Delta_{110} = 0.79$ eV)	0.4107 ($\Delta_{110} = 1.09$ eV)
$E_{\text{NM}}^{\text{DFT}}$	5.9319	5.9691 ($\Delta_{110} = 0.51$ eV)	5.9604 ($\Delta_{110} = 0.38$ eV)	6.0359 ($\Delta_{110} = 1.40$ eV)
$E_{\text{MC}}^{\text{DFT}}$	-5.6021	-5.6033	-5.5725	-5.6252
$E_{\text{MC}}^{\text{HH}}$	-1.7206	-1.7167 ($\Delta_{110} = 0.06$ eV)	-1.7071 ($\Delta_{110} = 0.18$ eV)	-1.7423 ($\Delta_{110} = -0.30$ eV)
E_{M}^{HH}	4.2113	4.2524 ($\Delta_{110} = 0.56$ eV)	4.2534 ($\Delta_{110} = 0.57$ eV)	4.2935 ($\Delta_{110} = 1.12$ eV)
$\sum A_i \mathbf{S}_i^2$	-7.7630	-7.7735	-7.7318	-7.6666
$\sum B_i \mathbf{S}_i^4$	5.6021	5.6034	5.5730	5.6257
E_{M}^{HL}	0.3298	0.3657 ($\Delta_{110} = 0.49$ eV)	0.3875 ($\Delta_{110} = 0.79$ eV)	0.4103 (1.09 eV)
$E_{\text{M}}^{\text{DFT}} - E_{\text{M}}^{\text{HL}}$	0.000	0.000	0.004	0.004

From DFT we expect it to be +0.79eV higher in energy than the $\langle 110 \rangle_D$, but we find that the energy difference is +0.57eV using the Heisenberg Hamiltonian.

We would like to understand the underlying reason for the relatively poor representation of the magnetic contribution delivered by the Heisenberg Hamiltonian. Figure 4 plots the orbitally projected density of states (PDOS) of the 3d-band electrons for the core α and the first n.n. β atoms for various SIA configurations. The PDOS are calculated using a $6 \times 6 \times 6$ MP k -point grid with the same parameters as given in Sec. II.

For bulk Fe at a_0^{DFT} , the orbitals at the Fermi energy (E_F) are predominantly t_{2g} states (see Fig. 5). We would expect the t_{2g} and e_g orbitals to contribute differently to the magnetic properties. In recent works by Kvashnin *et al.* [30] and A. Szilva *et al.* [32], an orbitally resolved analysis of exchange integrals of bcc Fe revealed that the t_{2g} orbitals are weakly dependent on the configuration of the spin moments and are *Heisenberg-like*, whereas the magnetic behavior of e_g states originates from double exchange.

With the exception of the $\langle 111 \rangle_D$ configuration, β site atoms have a PDOS similar to that in the bulk, while the PDOS of all the α site (core) atoms change significantly. For all the cases, a large van Hove singularity for the majority spin 3d electrons is observed to move into the conduction band. However, in the case of the $\langle 110 \rangle_D$, the Fermi energy is located at the peak in the PDOS of the $3d_{xz}$ and $3d_{xy}$ states, which is 0.5 eV lower than the maximum in the t_{2g} PDOS. In the case of $\langle 100 \rangle_D$, the $3d_{z^2}$ and $3d_{x^2-y^2}$ remain near the Fermi energy in the valence band, with the peak in the density of states of e_g orbitals moving into the conduction band. For the minority spin 3d electrons, a deep state at $E_F - 4$ eV develops, which is not present in the bulk. These deep-state electrons in the Fermi sea will not be easily excited and will not contribute to magnetic excitations, but they give rise to the suppression of magnetic moment at the core of SIA configurations.

The most important distinction in the PDOS calculations is that, unlike the other SIA configurations, the Fermi surface of the $\langle 111 \rangle_D$ is equally characterized by the t_{2g} and e_g orbitals.

Since the t_{2g} - t_{2g} interactions are responsible for the long-range RKKY-like exchange oscillations in Fe [30] along the $\langle 111 \rangle_D$ direction, the core situated along a $\langle 111 \rangle_D$ string will hinder the long-range oscillation across the chain due to the reduced t_{2g} occupation at E_F . e_g orbitals are known not to behave in a Heisenberg-like manner [30,32] but will contribute to the low-energy magnetic excitations. Therefore, it is clear that the Heisenberg Hamiltonian is unable to map the $\langle 111 \rangle_D$ magnetic contribution well due to the increased e_g occupation at the Fermi surface.

D. Self-consistent treatment of longitudinal fluctuations

The failure of the Heisenberg Hamiltonian arises due to the absence of the energy of formation of the magnetic moments in the model. Further, the MFT is derived in the long-wavelength limit where J_{ij} becomes unreliable due to the severe departure from the model approximation when magnetic moments become small. A possible approach to improve the magnetic description is to use an Anderson model which treats both the localized and itinerant characteristics on equal footing [97].

Alternatively one may incorporate longitudinal magnetic degrees of freedom using a Heisenberg-Landau Hamiltonian [20,21,66,67]:

$$\mathcal{H}_{HL} = \mathcal{H} + \sum_i (A_i \mathbf{S}_i^2 + B_i \mathbf{S}_i^4), \quad (17)$$

where A and B are the Landau coefficients and \mathcal{H} is the Heisenberg Hamiltonian as defined in Eq. (9). The Landau terms act to create a double well in the energy with respect to the magnitude of the magnetic moment. The well depth is the energy difference between the magnetic and nonmagnetic states. The minimum value is at the spontaneous magnetic moment $\mathbf{M}_{i,0} = -g\mu_B \mathbf{S}_{i,0}$ (Fig. 6).

While we use a real space representation in the current model, the Landau term is valid for arbitrary wave vectors when transformed into momentum space [98]. This distinguishes the Landau Hamiltonian from collinear magnetism

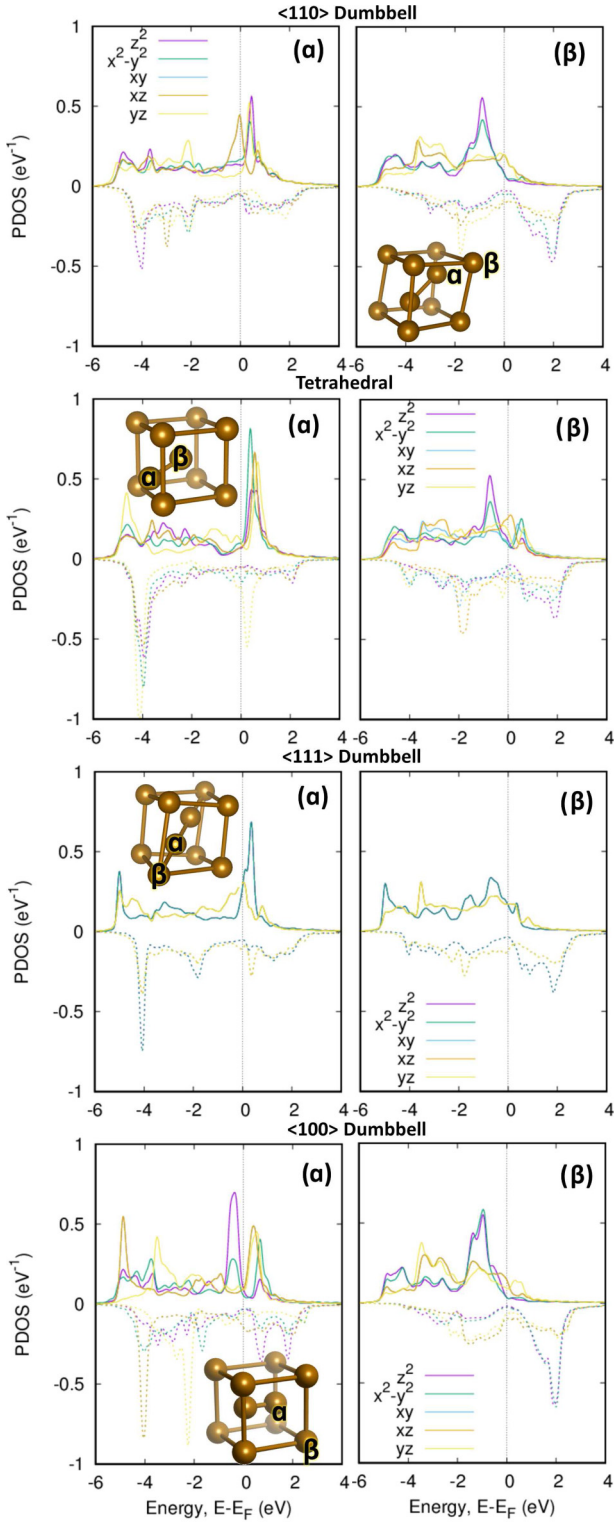


FIG. 4. Local orbitally projected density of states (PDOS) calculations for the core atoms (α) and their nearest neighbors (β) of various SIA configurations.

models. For example, the Stoner term in a collinear Stoner model ($-IM_{\mathbf{k}=0}^2/4$) neglects gains in the exchange energy that arise from spin fluctuations where $\mathbf{k} \neq 0$. Further, the presented model captures essential spin-spin correlations, which strongly affects properties interrelated by the fluctuation-

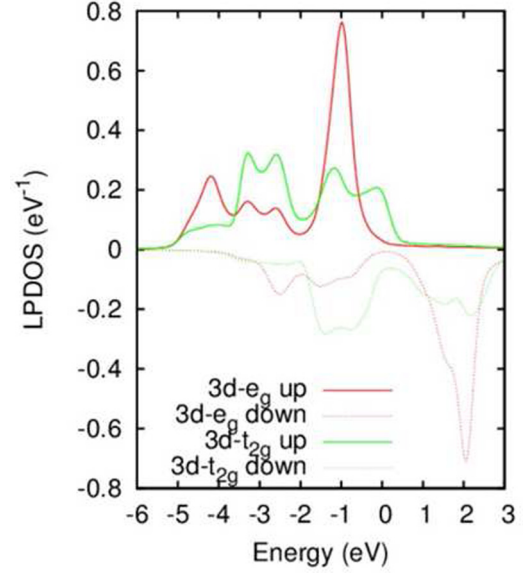


FIG. 5. Local partial density of states of bulk α -Fe. In bcc crystals, the $3d$ orbitals xy , xz , and yz are labeled t_{2g} while the $x^2 - y^2$ and $3z^2 - r^2$ are e_g .

dissipation theorem [12,98]. We should note that the magnetic moment in a Stoner or Stoner-like term can also be written as a vector variable or operator [99,100]. Hubbard-like Hamiltonians treat electronic structure directly, are based on a different concept than atomistic models, and are much more computationally demanding.

To determine the Landau parameters, we follow the logic presented in Ref. [23], where a single set of Landau parameters A and B were constructed for each simulation cell and then parametrized as a function of an effective electron density.

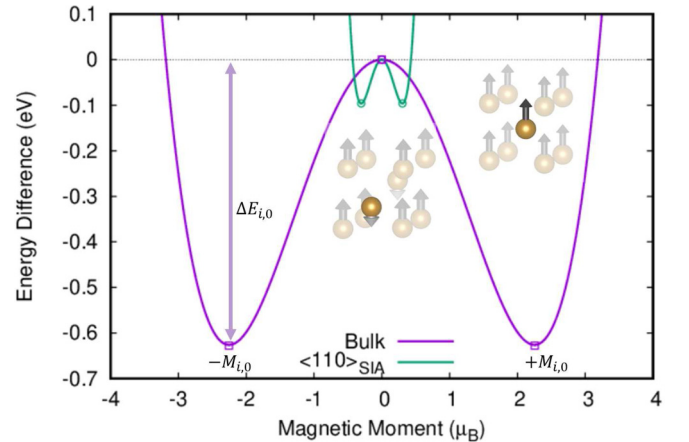


FIG. 6. The Landau part of energy as a function of the magnitude of magnetic moment. The double-well structure is a typical signature of the Landau Hamiltonian. We plotted the energy corresponding to the perfect lattice case and the energy of a core atom in a $\langle 110 \rangle$ dumbbell configuration. The spin-polarized DFT data are shown as points. The curves are drawn using the values of parameters $A'_i = -0.247$ and $B'_i = 0.02436$ for a bulk atom, and $A'_i = -2.093$ and $B'_i = 11.281$ for the $\langle 110 \rangle$ dumbbell, extracted using Eqs. (19) and (21).

Here, we generalize the approach to calculate a set of Landau coefficients for each atomic site.

We begin by defining a Landau Hamiltonian in which we only allow the atomic spin to contribute to the energy of its site i , such that we assume no inter-site Landau-type magnetic interactions. The atomic spins act as order parameters:

$$H'_{\text{HL}} = \sum_i (A'_i \mathbf{S}_i^2 + B'_i \mathbf{S}_i^4). \quad (18)$$

OPENMX allows us to calculate the energy components per site per orbital [68,101] due to the use of LCPAO (see Appendix B). One can calculate the energy difference for each atomic site between the magnetic and nonmagnetic configurations ΔE_i . Since we treat atomic spin as order parameters, the energy difference between any two states for site i can be expressed as

$$\Delta E_i = A'_i \mathbf{S}_{i,0}^2 + B'_i \mathbf{S}_{i,0}^4, \quad (19)$$

where $\mathbf{M}_{i,0} = -g\mu_B \mathbf{S}_{i,0}$ is the spontaneous magnetic moment. Knowing that the Landau Hamiltonian should have a minimum at the spontaneous magnetic moment, we are able to derive the moment in terms of the site-resolved Landau coefficients A'_i and B'_i :

$$\frac{\partial \Delta E_i}{\partial \mathbf{S}_{i,0}} = 0, \quad (20)$$

$$\Rightarrow S_{i,0} = |\mathbf{S}_{i,0}| = \sqrt{\frac{-A'_i}{2B'_i}} \neq 0. \quad (21)$$

For each atomic site we end up with a pair of simultaneous equations, i.e., Eqs. (19) and (21), from which we may determine the site-resolved Landau parameters.

We can then relate the primed Landau coefficients to those in the interacting Heisenberg-Landau Hamiltonian, which also includes the exchange coupling parameters. By equating Eqs. (17) and (18), we find

$$A_i \mathbf{S}_i = A'_i \mathbf{S}_i + \frac{1}{2} \sum_{j \neq i} J_{ij} \mathbf{S}_j, \quad (22)$$

$$= A'_i \mathbf{S}_i + \frac{1}{2} \mathbf{h}_i, \quad (23)$$

$$B_i = B'_i. \quad (24)$$

where

$$\mathbf{h}_i = -\frac{\partial \mathcal{H}}{\partial \mathbf{S}_i} = \sum_{j \neq i} J_{ij} \mathbf{S}_j, \quad (25)$$

which is the effective field of the Heisenberg Hamiltonian.

In Table VI we evaluate the contribution from the Landau part of the Hamiltonian for each SIA configurations. When the magnetic contribution of the Heisenberg-Landau mapping is added to the nonmagnetic DFT energy, the total energy is in excellent agreement with the spin-polarized DFT energy. The small relative error ($\approx 0.1\%$) in the Heisenberg-Landau energies with respect to DFT are well within the inherent error of DFT calculations.

In Fig. 7 we plot the resulting Landau coefficients defined according to Eqs. (23) and (24), using the values of J_{ij} calculated in Sec. III B. The site-resolved coefficients are plotted

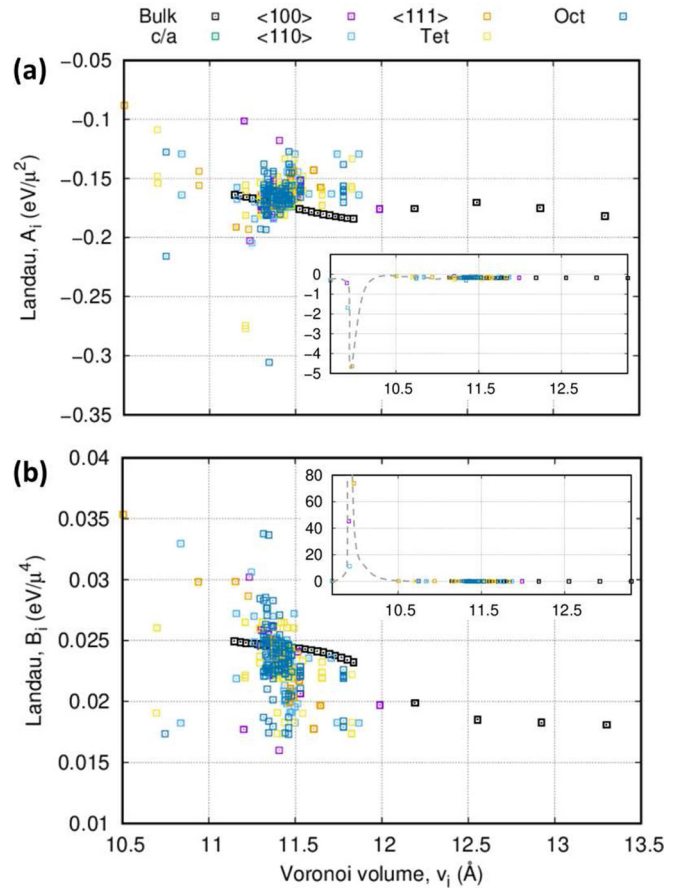


FIG. 7. Values of Landau parameters as a function of the Voronoi volume. Inset figures show the anomalously large values of the Landau terms for core atoms, resulting from the fact that magnetic moments are suppressed. Dashed lines guide the eye and have no interpretation.

against the local Voronoi volume calculated using the fuzzy cell partitioning method [102].

The site-resolved mapping confirms that Landau parameters do not form a simple relation with the Voronoi volume. Values of the Landau parameters change significantly for atoms in the core of defects. In Fig. 11 in Appendix A we also plot the Landau parameters with respect to a tight binding derived effective electron density used in many-body calculations and compare with values derived from a previous bulk definition [23]. Work is ongoing on the development of suitable descriptors to accurately represent exchange coupling parameters and Landau parameters with respect to the local environment, which represents a great challenge in the development of an accurate large-scale model combining magnetism and strong lattice deformations.

In this work, the second- and fourth-order Landau parameters were extracted from DFT calculations with the intent to improve the exchange-energy hypersurface of a spin-dynamics Hamiltonian when including strong lattice perturbing defects where the Heisenberg model becomes ill defined. However, the implementation of Landau parameters can also be considered a necessary inclusion for the study of perfect bcc or face-centered cubic (fcc) phases of iron without

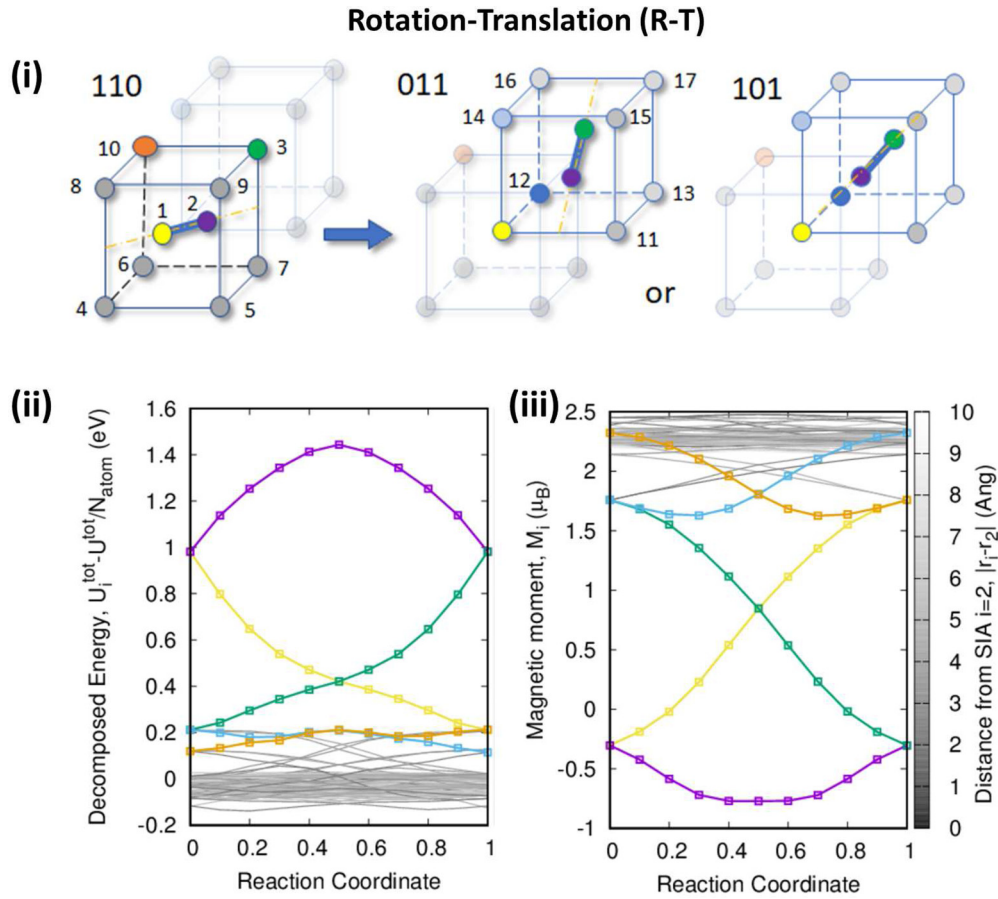


FIG. 8. Migration of $\langle 110 \rangle_D$ in α -Fe via Johnson's mechanism: rotation and translation. Part (i) shows a schematic of the transition paths. (ii) and (iii) display the site decomposed energy and magnetic moments, respectively, with selected atoms coloured according to (i). Energies in (ii) are translated relative to the average energy per atom ($U^{\text{tot}} = \langle U_i^{\text{tot}} \rangle$).

defects, not considered here [62,63]. Indeed, entirely independently, Refs. [23,54,48] identified that the correct assessment of phase stability requires the simultaneous treatment of lattice vibrations coupled with noncollinear excitations. When the magnon treatment included both longitudinal and transverse fluctuations the free energy differences were brought into the experimentally observed range. The presented method of extracting Landau terms can be used quite generally to improve the quantitative success of spin dynamics Hamiltonians when modeling iron and other ferromagnets.

E. Low energy migration pathways of atomic defects

In this section we consider the migration of a $\langle 110 \rangle_D$ via the two lowest energy pathways. Johnson's mechanism [103], a simultaneous rotation and translation of the dumbbell, has the lowest migration barrier. Our calculations value the barrier at 0.34 eV, in excellent quantitative agreement with previous DFT [26,93,104] and experimental [105] studies.

The next low energy pathway with a migration energy of 0.49 eV is the second n.n. jump mechanism. Schematic illustrations of the migration mechanisms are shown in panels (i) of Figs. 8 and 9. In addition, we show the decomposed energy (relative to the average atomic energy) and their respective magnetic moments during the transition in panels (ii) and

(iii), which are used in the calculation of the site-resolved Landau parameters. The energy decomposition identifies that the core atoms are approximately 1 eV more energetic than the average.

A third pathway, the translational jump, which migrates via an intermediate metastable $\langle 111 \rangle_D$ configuration is also known. Since it has a large migration energy of 0.79eV it is unfavorable and has not been considered below.

We may again observe how only using a Heisenberg Hamiltonian leads to erroneous results. In Fig. 10 we show the contribution to the effective field from the Heisenberg term during the rotation translation and second n.n. jumps of a $\langle 110 \rangle_D$. This interaction may be represented by means of an effective temperature $T_i = |\mathbf{h}_i|/k_B$. Without the Landau terms, core atoms are observed to have a *negative temperature* which is known to exist in nuclear spin systems [106]. This occurs as the magnetic moments on the core atoms oppose the effective field due to exchange interactions. However, the negative temperature is merely a consequence of the incompleteness of the Heisenberg model.

The Heisenberg-Landau Hamiltonian allows us to correctly account for the transverse fluctuations of magnetic moments in the vicinity of the core of SIA configurations. Since in this example the spin state of our model is fed directly from the DFT calculations which are in the adiabatic paradigm,

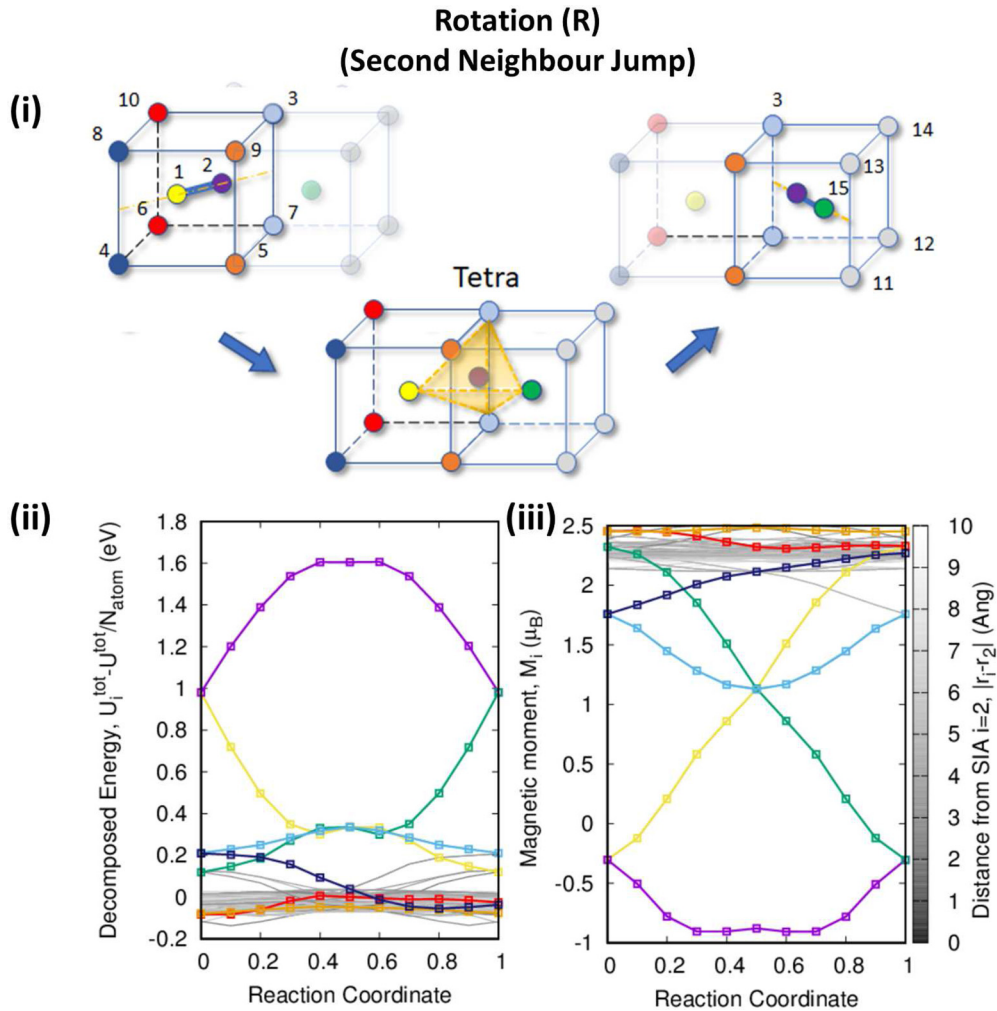


FIG. 9. Migration of $\langle 110 \rangle_D$ in α -Fe via a second neighbor jump: rotation. Part (i) shows a schematic of the transition paths. (ii) and (iii) display the site decomposed energy and magnetic moments, respectively, with selected atoms colored according to (i). Energies in (ii) are translated relative to the average energy per atom ($U^{\text{tot}} = \langle U_i^{\text{tot}} \rangle$).

we expect the effective field on each site to be zero (see the proof of this statement given in Appendix A). When in the ground state, the contribution to the effective magnetic field from the Landau terms acts to directly oppose those of the exchange such that the null condition is satisfied. We calculate the exchange coupling parameters and Landau coefficients for each NEB image and verify that the effective fields are zero as required. If the model is provided with an excited spin state, the effective fields are no longer vanishing and may be dynamically evolved [67].

IV. CONCLUSION

In this study, we explored the connection between first principles density functional calculations and the use of model Hamiltonians, to describe magnetic interactions in bcc iron containing structural defects. We benchmarked our LCPAO DFT results against literature data to verify the accuracy of calculations performed using the OPENMX code [68] and our own in-house exchange coupling code. We are able to correctly explain the known order of stability of self-interstitial

defects in magnetic Fe: $\langle 110 \rangle_D \rightarrow \text{tetrahedral} \rightarrow \langle 111 \rangle_{D/C} \rightarrow \langle 100 \rangle_D$, where the comparison of energies derived from magnetic and non-magnetic calculations reveals that magnetism causes the order of stability to change.

We explored the limits of validity of the commonly used Heisenberg Hamiltonian for the description of the magnetic interactions in iron containing defects. Exchange integrals were computed using the magnetic force theorem, allowing us to map the magnetic contribution onto the Heisenberg Hamiltonian functional form. When the mapped Heisenberg magnetic contribution is added to the nonmagnetic energies, the energy differences for the self-interstitial defects is reproduced within 10%. The self-interstitial configuration where the magnetic energy predicted using the Heisenberg Hamiltonian is the poorest is the $\langle 111 \rangle_D$ configuration. This occurs due to the increased population of the e_g orbitals at the Fermi energy.

Failures of the Heisenberg Hamiltonian can be mitigated by adding symmetry-breaking Landau terms to the magnetic Hamiltonian. By projecting energies onto atomic sites we generalize our earlier Heisenberg-Landau Hamiltonian [23] and define site-resolved Landau coefficients, determining the

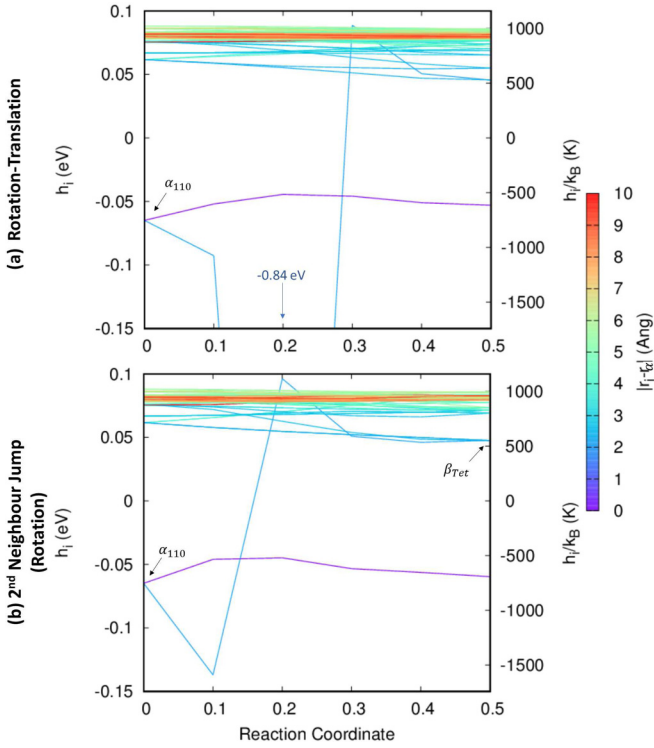


FIG. 10. Heisenberg effective field (and temperature) during the migration of a $\langle 110 \rangle_D$ dumbbell in bcc Fe.

values of these coefficients directly from the DFT calculations. We show that the Landau terms correct the magnetic energy contribution of the spin dynamics Hamiltonian and provides a significantly more accurate representation of energy hypersurfaces, matching magnetic DFT calculations. It remains unclear as to whether non-Heisenberg interactions truly exist in the physical system due to approximations involved in the MFT. This information is used for parametrizing a new generation of spin-lattice dynamics potentials. We further show how a Heisenberg Hamiltonian can lead to an incorrect interpretation of magnetism in the core of the defects, effectively corresponding to metastable “negative temperature” magnetic configurations in the core. These anomalies can be rectified using the Heisenberg-Landau Hamiltonian.

ACKNOWLEDGMENTS

We would like to express our gratitude to Max Boleininger and Andrew London for valuable discussions. This work has been carried out within the framework of the EUROfusion Consortium and has received funding from the Euratom Research and Training Programme 2014–2018 and 2019–2020 under Grant Agreement No. 633053. The views and opinions expressed herein do not necessarily reflect those of the European Commission. This work also received funding from the Euratom Research and Training Programme 2019–2020 under Grant Agreement No. 755039. We acknowledge funding by the RCUK Energy Programme (Grant No. EP/T012250/1), and EUROfusion for providing access to Marconi-Fusion HPC facility in the generation of data used in this paper.

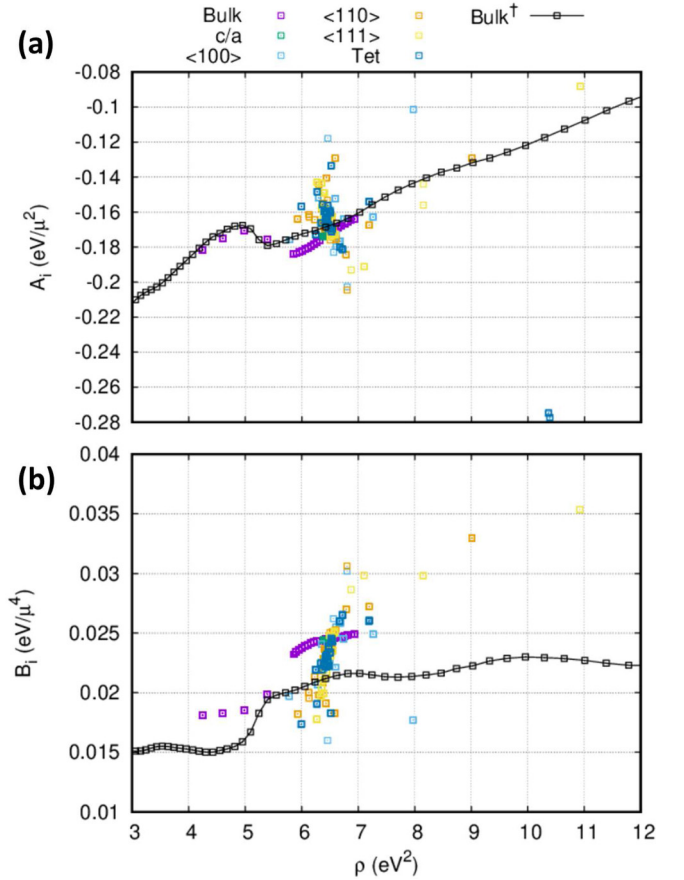


FIG. 11. Extracted Landau parameters as a function of local electron density as defined in Ref. [23]. The Landau parameters calculated for strained perfect bcc lattice from Ref. [23] are also shown for comparison (dagger).

APPENDIX A: EFFECTIVE FIELD OF HEISENBERG-LANDAU HAMILTONIAN

The effective field on an atomic site k in the configuration \mathcal{R} is a measure of the change in energy due to an infinitesimal change in the spin \mathbf{S}_k . In our construction of the Heisenberg-Landau Hamiltonian we allow for both transverse and longitudinal fluctuations of the semi-classical spin-vectors:

$$\mathbf{h}_k^{HL} = -\frac{\partial}{\partial \mathbf{S}_k} \mathcal{H}_{HL} \quad (\text{A1})$$

$$= \sum_{i \neq k} J_{ik} \mathbf{S}_i - 2A_k \mathbf{S}_k - 4B_k \mathbf{S}_k^3 \quad (\text{A2})$$

When in the electronic ground state, the changes in energy with respect to the spin should at be a minimum in the potential energy surface, thus requiring the effective field (the gradient of this potential) to be zero. This can be easily verified by substituting in the definitions of A_k and B_k from Eqs. (23) and (24). In a general spin-state this gives

$$\begin{aligned} \mathbf{h}_k^{HL} &= \sum_{i \neq k} J_{ik} \mathbf{S}_i - 2 \left(A'_k \mathbf{S}_k + \frac{1}{2} \sum_{j \neq k} J_{kj} \mathbf{S}_j \right) - 4B'_k \mathbf{S}_k^3 \\ &= -2A'_k \mathbf{S}_k - 4B'_k \mathbf{S}_k^3 = -\frac{\partial}{\partial \mathbf{S}_k} \mathcal{H}'_{HL}. \end{aligned} \quad (\text{A3})$$

Next we substitute A'_k for B'_k using Eq. (21):

$$\begin{aligned} \mathbf{h}_k^{HL} &= -2(-2B'_k \mathbf{S}_{k,0}^2) \mathbf{S}_k - 4B'_k \mathbf{S}_k^3 \\ &= 4B'_k (\mathbf{S}_{k,0}^2 - \mathbf{S}_k^2) \mathbf{S}_k. \end{aligned} \quad (\text{A4})$$

When the electronic orbitals are in their ground states for the atomic configuration, then so too will be the spin-order such that $\mathbf{S}_k \xrightarrow{GS} \mathbf{S}_{k,0}$:

$$\begin{aligned} \mathbf{h}_{k,0}^{HL} &= 4B'_k (\mathbf{S}_{k,0}^2 - \mathbf{S}_{k,0}^2) \mathbf{S}_{k,0} \\ &= \mathbf{0}. \end{aligned} \quad (\text{A5})$$

APPENDIX B: OPENMX ENERGY DECOMPOSITION

Due to the finite range of the pseudo-atomic orbitals in the pseudopotential based DFT formulation employed within the OPENMX code [68,101], the energy can be uniquely decomposed into contributions from each atomic site (i) and localized orbital (α):

$$E_{\text{tot}} = E_{\text{kin}} + E_{ec} + E_{ee} + E_{xc} + E_{cc} \quad (\text{B1})$$

$$= E_{\text{kin}} + (E_{ec}^{(L)} + E_{ec}^{(NL)}) + E_{ee} + E_{xc} + E_{cc}, \quad (\text{B2})$$

where the total energy terms are the kinetic energy (E_{kin}), electron-core Coulomb energy (E_{ec}), electron-electron Coulomb energy (E_{ee}), exchange correlation energy (E_{xc}), and the core-core Coulomb energy (E_{cc}). For practical and efficient implementation, OPENMX reorganizes the electron and core terms into two short-range terms and one long range term:

$$E_{\text{tot}} = E_{\text{kin}} + E_{xc} + E_{na} + E_{ec}^{(NL)} + E_{\delta ee} + E_{scc}. \quad (\text{B3})$$

Each term can be reduced into contributions from site and orbital indices:

$$E_{\text{tot}} = \sum_{i\alpha} E_{i\alpha}. \quad (\text{B4})$$

The kinetic energy operator can be decomposed as

$$E_{\text{kin}} = \sum_{\sigma} \sum_{i\alpha} \left(\sum_{j\beta} \sum_n \rho_{\sigma,i\alpha,j\beta}^{(\mathbf{R}_n)} h_{i\alpha,j\beta,kin}^{(\mathbf{R}_n)} \right) \quad (\text{B5})$$

$$= \sum_{\sigma} \sum_{i\alpha} E_{\sigma,i\alpha,kin}, \quad (\text{B6})$$

where the matrix elements of the kinetic energy operator are defined as

$$h_{i\alpha,j\beta,kin}^{(\mathbf{R}_n)} = \frac{1}{V_B} \int_{BZ} dk^3 \sum_{\mu}^{Occ} \langle \psi_{\sigma\mu}^{(\mathbf{k})} | \hat{T} | \psi_{\sigma\mu}^{(\mathbf{k})} \rangle. \quad (\text{B7})$$

The electron-core Coulomb terms are

$$E_{ec}^{(NL)} = \sum_{\sigma} \sum_{i\alpha} \left(\sum_n \sum_{j\beta} \rho_{\sigma,i\alpha,j\beta}^{(\mathbf{R}_n)} h_{i\alpha,j\beta,NL}^{(\mathbf{R}_n)} \right) \quad (\text{B8})$$

$$= \sum_{\sigma} \sum_{i\alpha} \left(\sum_n \sum_{j\beta} \rho_{\sigma,i\alpha,j\beta}^{(\mathbf{R}_n)} \langle \phi_{i\alpha} | \sum_I V_{NL,I} | \phi_{j\beta} \rangle \right) \quad (\text{B9})$$

$$= \sum_{\sigma} \sum_{i\alpha} E_{\sigma,i\alpha}^{(NL)}, \quad (\text{B10})$$

where V_{NL} is the nonlocal part of the pseudopotential.

The neutral atom term is

$$E_{na} = \int dr n(r) V_{na,I} \quad (\text{B11})$$

$$= \sum_{\sigma} \sum_{i\alpha} \left(\sum_{j\beta} \sum_n \rho_{\sigma,i\alpha,j\beta}^{(\mathbf{R}_n)} h_{i\alpha,j\beta,na}^{(\mathbf{R}_n)} \right) \quad (\text{B12})$$

$$= \sum_{\sigma} \sum_{i\alpha} E_{\sigma,i\alpha}^{na}. \quad (\text{B13})$$

The screened core correction is

$$E_{scc} = \frac{1}{2} \sum_{I,J} \left(\frac{Z_I Z_J}{|\tau_I - \tau_J|} - \int dr n_I^{(a)}(r) V_{H,J}^{(a)}(r) \right) \quad (\text{B14})$$

$$\begin{aligned} &= \sum_{\sigma} \sum_{i\alpha} \left(\frac{1}{2N_i} \sum_j \frac{Z_I Z_J}{|\tau_I - \tau_J|} \right. \\ &\quad \left. - \int dr n_I^{(a)}(r) V_{H,J}^{(a)}(r) \right) \end{aligned} \quad (\text{B15})$$

$$= \sum_{\sigma} \sum_{i\alpha} E_{\sigma,i\alpha}^{scc}. \quad (\text{B16})$$

The electron-electron Coulomb term is

$$E_{\delta ee} = \frac{1}{2} \int dr \left(n(r) - \sum_I n_I^{(a)}(r) \right) \delta V_H(r) \quad (\text{B17})$$

$$\begin{aligned} &= \sum_{\sigma} \sum_{i\alpha} \frac{1}{2} \left(\sum_{j\beta} \sum_n \rho_{\sigma,i\alpha,j\beta}^{(\mathbf{R}_n)} h_{i\alpha,j\beta}^{\delta V} \right. \\ &\quad \left. - \frac{1}{2} \int dr \frac{n_i^{(a)}(r)}{N_i} \delta V_H(r) \right) \end{aligned} \quad (\text{B18})$$

$$= \sum_{\sigma} \sum_{i\alpha} E_{\sigma,i\alpha}^{\delta ee}. \quad (\text{B19})$$

The exchange correlation term is

$$E_{xc} = \int dr [n(r) + n_{pcc}(r)] \epsilon_{xc}(r) \quad (\text{B20})$$

$$= \sum_{\sigma} \sum_{i\alpha} \left(\sum_n \sum_{j\beta} \rho_{\sigma,i\alpha,j\beta,xc}^{(\mathbf{R}_n)} h_{i\alpha,j\beta,xc}^{(\mathbf{R}_n)} \right) \quad (\text{B21})$$

$$+ \frac{1}{2N_i} \int dr n_{pcc,i}(r) \epsilon_{xc}(r) \quad (\text{B22})$$

$$= \sum_{\sigma} \sum_{i\alpha} E_{\sigma,i\alpha}^{xc}. \quad (\text{B23})$$

The proof of the decomposition for each term in the Kohn-Sham Hamiltonian [Eq. (B3)] can be found in the OPENMX developer material by Ozaki [101,107]. For completeness, we just copy their note here. Our reworked derivation is available upon request from the Culham Centre for Fusion Energy (CCFE) PublicationsManager@ukaea.uk.

Projections of nonlocal terms in the energy are treated as mean field. We confirm in this method the sum of the atomic

resolved energies is equivalent to the total energy in the Kohn-Sham DFT calculation.

This energy decomposition procedure provided the total energy per atomic site $E_i = \sum_{\alpha} E_{i\alpha}$ necessary to calculate the

site resolved Landau terms in Sec. III D. Figure 11 shows the Landau parameters calculated using this method as a function of local electron density in comparison to results from Ref. [23].

-
- [1] P. J. Hay, J. C. Thibeault, and R. J. Hoffmann, Orbital interactions in metal dimer complexes, *J. Am. Chem. Soc.* **97**, 4884 (1975).
- [2] T. J. Kim, H. Yoon, and M. J. Han, Calculating magnetic interactions in organic electrides, *Phys. Rev. B* **97**, 214431 (2018).
- [3] W. C. Lineberger and W. T. Borden, The synergy between qualitative theory, quantitative calculations, and direct experiments in understanding, calculating, and measuring the energy differences between the lowest singlet and triplet states of organic diradicals, *Phys. Chem. Chem. Phys.* **13**, 11792 (2011).
- [4] D. C. Jiles, *Introduction to Magnetism and Magnetic Materials* (CRC, Boca Raton, FL, 1998).
- [5] T. Shinjo, *Nanomagnetism and Spintronics* (Elsevier, Oxford, 2009).
- [6] S. Seki and M. Mochizuki, *Skyrmions and Magnetic Materials* (Springer, Cham, 2016).
- [7] W. Pepperhoff and M. Acet, *Constitution and Magnetism of Iron and its Alloys* (Springer, Berlin, 2010).
- [8] A. W. Overhauser, Spin density waves in an electron gas, *Phys. Rev.* **128**, 1437 (1962).
- [9] E. Fawcett, Spin-density-wave antiferromagnetism in chromium, *Rev. Mod. Phys.* **60**, 209 (1988).
- [10] S. K. Burke, R. Cywinski, J. R. Davis, and B. D. Rainford, The evolution of magnetic order in CrFe alloys. 2. Onset of ferromagnetism, *J. Phys. F* **13**, 451 (1983).
- [11] S. K. Burke and B. D. Rainford, The evolution of magnetic order in CrFe alloys: I. Antiferromagnetic alloys close to the critical concentration, *J. Phys. F* **13**, 441 (1983).
- [12] J. B. J. Chapman, P.-W. Ma, and S. L. Dudarev, Dynamics of magnetism in FeCr alloys with Cr clustering, *Phys. Rev. B* **99**, 184413 (2019).
- [13] C. W. Waggoner, A relation between the magnetic and elastic properties of a series of unhardened iron-carbon alloys, *Phys. Rev. (Ser. I)* **35**, 58 (1912).
- [14] K. Mergia and N. Boukos, Structural, thermal, electrical and magnetic properties of Eurofer 97 steel, *J. Nucl. Mater.* **373**, 1 (2008).
- [15] H. Hasegawa, M. W. Finnis, and D. G. Pettifor, A calculation of elastic constants of ferromagnetic iron at finite temperatures, *J. Phys. F* **15**, 19 (1985).
- [16] D. J. Dever, Temperature dependence of the elastic constants in α -iron single crystals: Relationship to spin order and diffusion anomalies, *J. Appl. Phys.* **43**, 3293 (1972).
- [17] V. I. Razumovskiy, A. V. Ruban, and P. A. Korzhavyi, Effect of Temperature on the Elastic Anisotropy of Pure Fe and Fe_{0.9}Cr_{0.1} Random Alloy, *Phys. Rev. Lett.* **107**, 205504 (2011).
- [18] H. Hasegawa and D. G. Pettifor, Microscopic Theory of the Temperature-Pressure Phase Diagram of Iron, *Phys. Rev. Lett.* **50**, 130 (1983).
- [19] F. Körmann, A. Dick, B. Grabowski, B. Hallstedt, T. Hickel, and J. Neugebauer, Free energy of bcc iron: Integrated *ab initio* derivation of vibrational, electronic, and magnetic contributions, *Phys. Rev. B* **78**, 033102 (2008).
- [20] M. Yu. Lavrentiev, D. Nguyen-Manh, and S. L. Dudarev, Magnetic cluster expansion model for bcc-fcc transitions in Fe and Fe-Cr alloys, *Phys. Rev. B* **81**, 184202 (2010).
- [21] M. Yu. Lavrentiev, R. Soulaïrol, C. C. Fu, D. Nguyen-Manh, and S. L. Dudarev, Noncollinear magnetism at interfaces in iron-chromium alloys: The ground states and finite-temperature configurations, *Phys. Rev. B* **84**, 144203 (2011).
- [22] F. Körmann, T. Hickel, and J. Neugebauer, Influence of magnetic excitations on the phase stability of metals and steels, *Curr. Opin. Solid State Mater. Sci.* **20**, 77 (2016).
- [23] P.-W. Ma, S. L. Dudarev, and J. S. Wrobel, Dynamic simulation of structural phase transitions in magnetic iron, *Phys. Rev. B* **96**, 094418 (2017).
- [24] D. Nguyen-Manh, A. P. Horsfield, and S. L. Dudarev, Self-interstitial atom defects in bcc transition metals: Group-specific trends, *Phys. Rev. B* **73**, 020101(R) (2006).
- [25] P. M. Derlet, D. Nguyen-Manh, and S. L. Dudarev, Multiscale modeling of crowdion and vacancy defects in body-centered-cubic transition metals, *Phys. Rev. B* **76**, 054107 (2007).
- [26] P.-W. Ma and S. L. Dudarev, Universality of point defect structure in body-centered cubic metals, *Phys. Rev. Materials* **3**, 013605 (2019).
- [27] S. Blundell, *Magnetism in Condensed Matter*, Oxford Master Series in Condensed Matter Physics (Oxford, University Press, Oxford, 2001).
- [28] A. I. Lichtenstein, M. I. Katsnelson, V. P. Antropov, and V. A. Gubanov, Local spin density functional approach to the theory of exchange interactions in ferromagnetic materials and alloys, *J. Magn. Magn. Mater.* **67**, 65 (1987).
- [29] T. Steenbock, J. Tasche, A. I. Lichtenstein, and C. Herrmann, A Greens-function approach to exchange spin coupling as a new tool for quantum chemistry, *J. Chem. Theory Comput.* **11**, 5651 (2015).
- [30] Y. O. Kvashnin, R. Cardias, A. Szilva, I. Di Marco, M. I. Katsnelson, A. I. Lichtenstein, L. Nordström, A. B. Klautau, and O. Eriksson, Microscopic Origin of Heisenberg and Non-Heisenberg Exchange Interactions in Ferromagnetic bcc Fe, *Phys. Rev. Lett.* **116**, 217202 (2016).
- [31] A. Szilva, M. Costa, A. Bergman, L. Szunyogh, L. Nordström, and O. Eriksson, Interatomic Exchange Interactions for Finite-Temperature Magnetism and Nonequilibrium Spin Dynamics, *Phys. Rev. Lett.* **111**, 127204 (2013).
- [32] A. Szilva, D. Thonig, P. F. Bessarab, Y. O. Kvashnin, D. C. M. Rodrigues, R. Cardias, M. Pereiro, L. Nordström, A. Bergman, A. B. Klautau, and O. Eriksson, Theory of noncollinear interactions beyond Heisenberg exchange: Applications to bcc Fe, *Phys. Rev. B* **96**, 144413 (2017).
- [33] D. M. Korotin, V. V. Mazurenko, V. I. Anisimov, and S. V. Streltsov, Calculation of exchange constants of the

- Heisenberg model in plane-wave-based methods using the Green's function approach, *Phys. Rev. B* **91**, 224405 (2015).
- [34] R. Cardias, A. Szilva, A. Bergman, I. Di Marco, M. I. Katsnelson, A. I. Lichtenstein, L. Nordström, A. B. Klautau, O. Eriksson, and Y. O. Kvashnin, The Bethe-Slater curve revisited: New insights from electronic structure theory, *Sci. Rep.* **7**, 4058 (2017).
- [35] S. Trtica, H. Prosenc M, M. Schmidt, J. Heck, O. Albrecht, D. G. F. Reuter, and E. Rentschler, Stacked nickelocenes: Synthesis, structural characterization, and magnetic properties, *Inorg. Chem.* **49**, 1667 (2010).
- [36] A. Abedi, N. Safari, V. Amani, and H. R. Khavasi, Synthesis, characterization, mechanochromism and photochromism of $[\text{Fe}(\text{dm4bt})_3][\text{FeCl}_4]_2$ and $[\text{Fe}(\text{dm4bt})_3][\text{FeBr}_4]_2$, along with the investigation of steric influence on spin state, *Dalton Trans.* **40**, 6877 (2011).
- [37] O. K. Andersen and O. Jepsen, Explicit, First-Principles Tight-Binding Theory, *Phys. Rev. Lett.* **53**, 2571 (1984).
- [38] M. van Schilfgaarde and V. P. Antropov, First-principles exchange interactions in Fe, Ni and Co, *J. Appl. Phys.* **85**, 4827 (1999).
- [39] L.-S. Xie, G.-X. Jin, L. He, G. E. W. Bauer, J. Barker, and K. Xia, First-principles study of exchange interactions of yttrium iron garnet, *Phys. Rev. B* **95**, 014423 (2017).
- [40] S. H. Liu, Quasispin model of itinerant magnetism: High-temperature theory, *Phys. Rev. B* **15**, 4281 (1977).
- [41] R. E. Prange and V. Korenman, Local-band theory of itinerant ferromagnetism. IV. Equivalent Heisenberg model, *Phys. Rev. B* **19**, 4691 (1979).
- [42] C. S. Wang, R. E. Prange, and V. Korenman, Magnetism in iron and nickel, *Phys. Rev. B* **25**, 5766 (1982).
- [43] A. I. Lichtenstein, M. I. Katnelson, and V. A. Gubanov, Exchange interactions and spin-wave stiffness in ferromagnetic materials, *J. Phys. F* **14**, L125 (1984).
- [44] T. Oguchi, K. Terakura, and N. Hamada, Magnetism of iron above the Curie temperature, *J. Phys. F* **13**, 145 (1983).
- [45] P. Bruno, Exchange Interaction Parameters and Adiabatic Spin-Wave Spectra of Ferromagnets: A Renormalized Magnetic Force Theorem, *Phys. Rev. Lett.* **90**, 087205 (2003).
- [46] H. Yoon, T. J. Kim, J.-H. Sim, S. W. Jang, T. Ozaki, and M. J. Han, Reliability and applicability of magnetic-force linear response theory: Numerical parameters, predictability, and orbital resolution, *Phys. Rev. B* **97**, 125132 (2018).
- [47] M. J. Han, T. Ozaki, and J. Yu, Electronic structure, magnetic interactions, and the role of ligands in Mn_n ($n = 4, 12$) single-molecule magnets, *Phys. Rev. B* **70**, 184421 (2004).
- [48] A. A. Katanin, A. S. Belozеров, and V. I. Anisimov, Nonlocal correlations in the vicinity of the α - γ phase transition in iron within a DMFT plus spin-fermion model approach, *Phys. Rev. B* **94**, 161117(R) (2016).
- [49] A. S. Belozеров, A. A. Katanin, and V. I. Anisimov, Momentum-dependent susceptibilities and magnetic exchange in bcc iron from supercell DMFT calculations, *Phys. Rev. B* **96**, 075108 (2017).
- [50] M. I. Katsnelson and A. I. Lichtenstein, First-principles calculations of magnetic interactions in correlated systems, *Phys. Rev. B* **61**, 8906 (2000).
- [51] R. F. L. Evans, W. J. Fan, P. Chureemart, T. A. Ostler, M. O. A. Ellis, and R. W. Chantrell, Atomistic spin model simulations of magnetic nanomaterials, *J. Phys.: Condens. Matter* **26**, 103202 (2014).
- [52] J. Tranchida, S. J. Plimpton, P. Thilbaudeau, and A. P. Thompson, Massively parallel symplectic algorithm for coupled magnetic spin dynamics and molecular dynamics, *J. Comput. Phys.* **372**, 406 (2018).
- [53] P.-W. Ma, S. L. Dudarev, A. A. Semenov, and C. H. Woo, Temperature for a dynamic spin ensemble, *Phys. Rev. E* **82**, 031111 (2010).
- [54] M. Y. Lavrentiev, D. Nguyen-Manh, and S. L. Dudarev, Cluster expansion models for Fe-Cr alloys, the prototype materials for a fusion power plant, *Comput. Mater. Sci.* **49**, S199 (2010).
- [55] D. W. Boukhvalov, A. I. Lichtenstein, V. V. Dobrovitski, M. I. Katsnelson, B. N. Harmon, V. V. Mazurenko, and V. I. Anisimov, Effect of local Coulomb interactions on the electronic structure and exchange interactions in Mn_{12} magnetic molecules, *Phys. Rev. B* **65**, 184435 (2002).
- [56] D. W. Boukhvalov, V. V. Dobrovitski, M. I. Katsnelson, A. I. Lichtenstein, B. N. Harmon, and P. Kögerler, Electronic structure and exchange interactions in V_{15} magnetic molecules: LDA+U results, *Phys. Rev. B* **70**, 054417 (2004).
- [57] D. W. Boukhvalov, Yu. N. Gornostyrev, M. I. Katsnelson, and A. I. Lichtenstein, Magnetism and Local Distortions Near Carbon Impurity in γ -Iron, *Phys. Rev. Lett.* **99**, 247205 (2007).
- [58] G. S. Chang, E. Z. Kurmaev, D. W. Boukhvalov, L. D. Finkelstein, S. Colis, T. M. Pedersen, A. Moewes, and A. Dinia, Effect of Co and O defects on the magnetism in Co-doped ZnO: Experiment and theory, *Phys. Rev. B* **75**, 195215 (2007).
- [59] R. Cardias, M. M. Bezerra-Neto, M. S. Ribeiro, A. Bergman, A. Szilva, O. Eriksson, and A. B. Klautau, Magnetic and electronic structure of Mn nanostructures on Ag(111) and Au(111), *Phys. Rev. B* **93**, 014438 (2016).
- [60] R. Drautz and M. Fähnle, Parametrization of the magnetic energy at the atomic level, *Phys. Rev. B* **72**, 212405 (2005).
- [61] S. V. Okatov, Yu. N. Gornostyrev, A. I. Lichtenstein, and M. I. Katsnelson, Magnetoelastic coupling in γ -iron investigated within an *ab initio* spin spiral approach, *Phys. Rev. B* **84**, 214422 (2011).
- [62] R. Singer, F. Dietermann, and M. Fähnle, Spin Interactions in bcc and fcc Fe Beyond the Heisenberg Model, *Phys. Rev. Lett.* **107**, 017204 (2011).
- [63] R. Singer, F. Dietermann, and M. Fähnle, Erratum: Spin interactions in bcc and fcc Fe Beyond the Heisenberg Model, *Phys. Rev. Lett.* **107**, 119901(E) (2011).
- [64] A. V. Ruban, S. Khmelevskiy, P. Mohn, and B. Johansson, Temperature-induced longitudinal spin fluctuations in Fe and Ni, *Phys. Rev. B* **75**, 054402 (2007).
- [65] P.-W. Ma and S. L. Dudarev, Longitudinal magnetic fluctuations in Langevin spin dynamics, *Phys. Rev. B* **86**, 054416 (2012).
- [66] P. M. Derlet, Landau-Heisenberg Hamiltonian model for FeRh, *Phys. Rev. B* **85**, 174431 (2012).
- [67] P.-W. Ma and S. L. Dudarev, Atomistic spin-lattice dynamics, in *Handbook of Materials Modeling: Methods: Theory and Modeling*, edited by W. Andreoni and S. Yip (Springer, Cham, 2020), pp. 1017–1035.
- [68] T. Ozaki, H. Kino, J. Yu, M.J. Han M. Ohfuchi, F. Ishii, K. Sawada, Y. Kubota, Y.P. Mizuta, T. Ohwaki, T.V.T. Duy, H. Weng, Y. Shiihara, M. Toyoda, Y. Okuno, R. Perez, P.P. Bell,

- M. Ellner, Yang Xiao, A.M. Ito, M. Kawamura, K. Yoshimi, C.-C. Lee, Y.-T. Lee, M. Fukuda, and K. Terakura, <http://www.openmx-square.org/> (2003).
- [69] J. P. Perdew, K. Burke, and M. Ernzerhof, Generalized Gradient Approximation Made Simple, *Phys. Rev. Lett.* **77**, 3865 (1996).
- [70] J. P. Perdew, K. Burke, and M. Ernzerhof, Erratum: Generalized Gradient Approximation Made Simple, *Phys. Rev. Lett.* **78**, 1396(E) (1997).
- [71] T. Ozaki, Variationally optimized atomic orbitals for large-scale electronic structures, *Phys. Rev. B* **67**, 155108 (2003).
- [72] T. Ozaki and H. Kino, Numerical atomic basis orbitals from H to Kr, *Phys. Rev. B* **69**, 195113 (2004).
- [73] T. Ozaki and H. Kino, Efficient projector expansion for the *ab initio* LCAO method, *Phys. Rev. B* **72**, 045121 (2005).
- [74] H. J. Monkhorst and J. D. Pack, Special points for Brillouin-zone integrations, *Phys. Rev. B* **13**, 5188 (1976).
- [75] P. E. Blöchl, Generalized separable potentials for electronic-structure calculations, *Phys. Rev. B* **41**, 5414(R) (1990).
- [76] I. Morrison, D. M. Bylander, and L. Kleinman, Nonlocal Hermitian norm-conserving Vanderbilt pseudopotential, *Phys. Rev. B* **47**, 6728 (1993).
- [77] G. Kresse and J. Hafner, *Ab initio* molecular dynamics for liquid metals, *Phys. Rev. B* **47**, 558(R) (1993).
- [78] G. Kresse and J. Hafner, *Ab initio* molecular-dynamics simulation of the liquid-metal–amorphous-semiconductor transition in germanium, *Phys. Rev. B* **49**, 14251 (1994).
- [79] G. Kresse and J. Furthmüller, Efficiency of *ab initio* total energy calculations for metals and semiconductors using a plane-wave basis set, *Comput. Mater. Sci.* **6**, 15 (1996).
- [80] G. Kresse and J. Furthmüller, Efficient iterative schemes for *ab initio* total-energy calculations using a plane-wave basis set, *Phys. Rev. B* **54**, 11169 (1996).
- [81] P. Olsson, C. Domain, and J. Wallenius, *Ab initio* study of Cr interactions with point defects in bcc Fe, *Phys. Rev. B* **75**, 014110 (2007).
- [82] M. Pajda, J. Kudrnovský, I. Turek, V. Drchal, and P. Bruno, *Ab initio* calculations of exchange interactions, spin-wave stiffness constants, and Curie temperatures of Fe, Co, and Ni, *Phys. Rev. B* **64**, 174402 (2001).
- [83] I. Turek, J. Kudrnovský, V. Drchal, and P. Bruno, Exchange interactions, spin waves, and transition temperatures in itinerant magnets, *Philos. Mag.* **86**, 1713 (2006).
- [84] P. Lloyd and P. V. Smith, Multiple scattering theory in condensed materials, *Adv. Phys.* **21**, 69 (1972).
- [85] A. Terasawa, M. Matsumoto, T. Ozaki, and Y. Gohda, Efficient algorithm based on liechtenstein method for computing exchange coupling constants using localised basis set, *J. Phys. Soc. Jpn.* **88**, 114706 (2019).
- [86] Charles Kittel, *Introduction to Solid State Physics*, 8th ed. (Wiley, New York, 2004).
- [87] J. A. Rayne and B. S. Chandrasekhar, Elastic constants of iron from 4.2 to 300 K, *Phys. Rev.* **122**, 1714 (1961).
- [88] H. Wang, P.-W. Ma, and C. H. Woo, Exchange interaction for spin-lattice coupling in bcc iron, *Phys. Rev. B* **82**, 144304 (2010).
- [89] J. S. Wróbel, D. Nguyen-Manh, M. Y. Lavrentiev, M. Muzyk, and S. L. Dudarev, Phase stability of ternary fcc and bcc Fe-Cr-Ni alloys, *Phys. Rev. B* **91**, 024108 (2015).
- [90] M. Acet, H. Zähres, E. F. Wassermann, and W. Pepperhoff, High-temperature moment-volume instability and anti-Invar of γ -Fe, *Phys. Rev. B* **49**, 6012 (1994).
- [91] S. Frota-Pessôa, R. B. Muniz, and J. Kudrnovský, Exchange coupling in transition-metal ferromagnets, *Phys. Rev. B* **62**, 5293 (2000).
- [92] C. Domain and C. S. Becquart, *Ab initio* calculations of defects in Fe and dilute Fe-Cu alloys, *Phys. Rev. B* **65**, 024103 (2001).
- [93] C. C. Fu, F. Willaime, and P. Ordejón, Stability and Mobility of Mono- and Di-Interstitials in α -Fe, *Phys. Rev. Lett.* **92**, 175503 (2004).
- [94] F. Willaime, C. C. Fu, M. C. Marinica, and J. Dalla Torre, Stability and mobility of self-interstitials and small interstitial clusters in α -iron: *Ab initio* and empirical potential calculations, *Nucl. Instrum. Methods Phys. Res. B* **228**, 92 (2005).
- [95] C. S. Becquart, R. Ngayam Happy, P. Olsson, and C. Domain, A DFT study of the stability of SIA and small SIA clusters in the vicinity of solute atoms in Fe, *J. Nucl. Mater.* **500**, 92 (2018).
- [96] M.-C. Marinica, F. Willaime, and J.-P. Crocombette, Irradiation-Induced Formation of Nanocrystallites with C15 Laves Phase Structure in bcc Iron, *Phys. Rev. Lett.* **108**, 025501 (2012).
- [97] D. Nguyen-Manh and S. L. Dudarev, Model many-body Stoner Hamiltonian for binary FeCr alloys, *Phys. Rev. B* **80**, 104440 (2009).
- [98] T. Moriya, A unified theory and its general consequences, in *Spin Fluctuations in Itinerant Electron Magnetism* (Springer, Berlin, 1985), pp. 129–156.
- [99] M. E. A. Coury, S. L. Dudarev, W. M. C. Foulkes, A. P. Horsfield, P.-W. Ma, and J. S. Spencer, Hubbard-like Hamiltonians for interacting electrons in *s*, *p*, and *d* orbitals, *Phys. Rev. B* **93**, 075101 (2016).
- [100] M. E. A. Coury, S. L. Dudarev, W. M. C. Foulkes, A. P. Horsfield, P.-W. Ma, and J. S. Spencer, Erratum: Hubbard-like Hamiltonians for interacting electrons in *s*, *p*, and *d* orbitals, *Phys. Rev. B* **98**, 039904(E) (2018).
- [101] T. Ozaki, http://www.openmx-square.org/workshop/meeting15/OpenMX_Resolved.pdf (2018).
- [102] A. D. Becke and R. M. Dickson, Numerical solution of Poisson's equation in polyatomic molecules, *J. Chem. Phys.* **89**, 2993 (1988).
- [103] R. A. Johnson, Interstitials and vacancies in α -iron, *Phys. Rev.* **134**, A1329 (1964).
- [104] C.-C. Fu, J. D. Torre, F. Willaime, J.-L. Bocquet, and A. Barbu, Multiscale modelling of defect kinetics in irradiated iron, *Nat. Mater.* **4**, 68 (2005).
- [105] P. Ehrhart, P. Jung, H. Schultz, and H. Ullmaier, in *Atomic Defects in Metals*, Landolt-Börnstein, Group III, Condensed Matter Vol. 25, edited by H. Ullmaier (Springer, Berlin, 1991).
- [106] E. M. Purcell and R. V. Pound, A nuclear spin system at negative temperature, *Phys. Rev.* **81**, 279 (1951).
- [107] T. Ozaki, <http://www.openmx-square.org/workshop/meeting15/>